Nature Communications

https://doi.org/10.1038/s41467-026-69978-w

Article in Press

Structural heterogeneity and substrate engagement mechanism of the bacterial proteasome activator Bpa

Received: 21 September 2025

Accepted: 16 February 2026

Cite this article as: Davis, B.T., Rennella, E., Haris, A. *et al.* Structural heterogeneity and substrate engagement mechanism of the bacterial proteasome activator Bpa. *Nat Commun* (2026). https://doi.org/10.1038/s41467-026-69978-w

Bradley T. V. Davis, Enrico Rennella, Anisha Haris, Jakub Ujma, David Bruton, Keith Richardson, Kevin Giles, Lewis E. Kay & Siavash Vahidi

Structural heterogeneity and substrate engagement mechanism of the bacterial proteasome activator Bpa

Bradley T. V. Davis[1†], Enrico Rennella[2†], Anisha Haris[3], Jakub Ujma[3], David Bruton[3], Keith Richardson[3], Kevin Giles[3], Lewis E. Kay[2,4,5,6*], Siavash Vahidi[1*]

[1]Department of Cellular and Molecular Biology, University of Guelph, Guelph, Ontario, N1G 2W1, Canada

[2]Department of Molecular Genetics, University of Toronto, Toronto, Ontario, M5S 1A8, Canada

[3]Waters Corporation, Stamford Avenue, Altrincham Road, Wilmslow, SK9 4AX, U.K.

[4]Department of Biochemistry, University of Toronto, Toronto, Ontario, M5S 1A8, Canada

[5]Department of Chemistry, University of Toronto, Toronto, Ontario, M5S 1A8, Canada

[6]Program in Molecular Medicine, Hospital for Sick Children, Toronto, Ontario, M5G 1X8, Canada

† These authors contributed equally.

*Correspondence to: svahidi@uoguelph.ca; lewis.kay@utoronto.ca

Abstract

Bacterial proteasomal activator (Bpa) is a regulatory particle of the *Mycobacterium tuberculosis* proteasome that facilitates the recruitment of substrates and their subsequent degradation by the 20S core particle. Substrate-bound structures of Bpa are unavailable, leaving its recruitment mechanism incompletely understood. Here, we use mass spectrometry and NMR to show that Bpa reversibly assembles into dodecamers from dimers/tetramers in a temperature-dependent manner in vitro, and map the oligomerization interfaces during assembly. To overcome the limitations posed by the poor solubility of natural Bpa substrates, we establish the DNA-binding domain of hTRF1 as a model substrate. We quantify the affinity and stoichiometry of the Bpa-hTRF1 interaction using methyl-TROSY NMR, identifying a 12 Bpa subunit: 3 hTRF1 binding ratio with micromolar affinity that is modulated by salt concentration. Our work maps the Bpa-hTRF1 interface at atomic resolution, identifies determinants of substrate engagement, and introduces a tractable substrate for dissecting proteasomal recognition in mycobacteria.

Introduction

Mycobacterium tuberculosis (*Mtb*) uses a rare prokaryotic proteasome system to resist nitrosative and oxidative toxicity in host macrophages[1,2]. Thus, the *Mtb* proteasome and its interacting partners are novel therapeutic targets for developing antibacterials against multidrug-resistant *Mtb*[3–5]. The *Mtb* 20S core particle (CP) consists of an assembly of homoheptameric rings, arranged in a α_7-β_7-β_7-α_7 architecture, that sequesters fourteen catalytic sites, one within each β-subunit (Fig. 1a). Proteasomal activity is tightly controlled by a gating mechanism within the α_7-rings[6]. As a result, the 20S CP alone can only degrade small, unstructured substrates that are able to passively diffuse through the closed gate. Activation of the 20S CP requires the

binding of unstructured C-terminal GQYL motifs of regulatory particles (RPs) to an α_7-ring, triggering gate opening and enabling substrate entry[6–9] (Fig. 1b). RPs also engage, unfold, and translocate substrates into the 20S CP for degradation. *Mtb* encodes two known RPs that interact with the 20S CP: Mpa, and Bpa[7,10–14]. The hexameric, ATP-dependent RP Mpa (Mycobacterial proteasome ATPase; Rv2115c), unfolds and translocates pupylated substrates into the 20S CP for degradation. In contrast, the Bpa (Bacterial proteasome activator; Rv3780) RP functions independently of the pupylation pathway and mediates the degradation of a distinct set of substrates in an ATP-independent fashion[7,12]. Bpa is essential for *Mtb* persistence under heat shock and oxidative stress by degrading, among other substrates[7,11], HspR (Heat-shock protein repressor; Rv0353), a transcriptional repressor of the dnaKJ-grpE-hspR operon[2,12,15,16]. Under heat shock, HspR dissociates from the HspR-associated inverted repeat DNA sequence (HAIR) motif and from DnaK, exposing it for Bpa-mediated proteasomal degradation[2,17]. While Mpa's substrate recruitment is well characterized[18–20], the substrate recognition mechanism of Bpa remains incompletely understood, with HspR the only well-established natural substrate characterized to date[2,11,15].

Elegant structural studies have elucidated the architecture of substrate-free (apo) Bpa[12] and its binding mechanism to the 20S CP[13,21]. Each Bpa subunit is comprised of a four-helix bundle that oligomerizes into a 228-kDa homododecameric ring[11,12] (Figs. 1c, d). The stability of dodecameric Bpa depends on inter-subunit contacts mediated by the H0 helix and a GXXXGXXXG motif in H4 that packs against H1/H4 of the neighbouring subunit[11,12]. Two aspects of Bpa structure and function remain incompletely understood: the solution-state structural heterogeneity of Bpa and the molecular basis of substrate recognition. von Rosen et al.[2] used mutagenesis and biochemical assays to show that Bpa recognizes HspR via a bipartite mechanism: the N-terminal DNA-binding helix-turn-helix (HTH) domain provides stable binding

to Bpa, while the C-terminal disordered, sequence-specific tail acts as a threading motif that initiates translocation and promotes efficient 20S CP turnover. This indicates, that at least for HspR, intrinsic disorder alone is insufficient for Bpa recruitment, and that both structural and sequence features are critical for substrate selection. In subsequent work[21], the same group used cross-linking mass spectrometry and electron cryomicroscopy (cryo-EM) of chemically-crosslinked Bpa-HspR complexes to implicate Bpa residues H131, F138, and R145 in substrate binding. Substantial heterogeneity in Bpa-HspR complexes precluded structure determination, leaving the precise binding interface between Bpa and its substrates unresolved.

Here, using a combination of mass spectrometry (MS)- and nuclear magnetic resonance (NMR) spectroscopy-based tools, we map the dynamic interfaces that mediate Bpa oligomerization and substrate recognition in vitro. By leveraging a model substrate, we show that Bpa recognizes short hydrophobic motifs embedded within disordered regions of substrates. This interaction is mediated through solvent-accessible hydrophobic bands on the inner surface of the Bpa dodecameric ring, is modulated by ionic strength, and exhibits defined stoichiometry. Our proposed substrate engagement mechanism provides testable hypotheses for natural substrates and offers broader implications for understanding regulated proteolysis across mycobacteria.

Results

Bpa undergoes temperature-dependent oligomerization

We heterologously expressed and purified wild-type (WT) *Mtb* Bpa. In the process of purification optimization, we observed a striking temperature-dependent shift in elution profiles during the final size exclusion chromatography (SEC) step. Samples incubated at 4 °C displayed a different

chromatographic peak distribution compared to those incubated at 37 °C, consistent with changes in particle size. To quantify this process, we incubated Bpa at 37 °C following extended storage at 4 °C and analyzed Bpa particle size at defined time intervals by SEC. Chromatograms revealed three distinct peaks corresponding to a high-molecular weight assembly (P1) and two lower-molecular weight species (P2 and P3), whose relative abundances changed with incubation time (Fig. 1e). At the onset of incubation at 37 °C, the chromatograms were dominated by the smaller P2 and P3 species. These species progressively converted to the larger P1 species over time. We quantified this transition by integrating each peak and fitting the increase in P1 abundance using a first-order exponential model, yielding an apparent rate constant k_{SEC} of 0.35 ± 0.04 h^{-1} (Fig. 1f). We extended this analysis to intermediate temperatures and measured Bpa assembly following extended storage at 4 °C and transfer to 15 °C or 25 °C. We measured k_{SEC} of 0.06 ± 0.01 h^{-1} for the 4 to 25 °C transition, and k_{SEC} of 0.03 ± 0.01 h^{-1} for the 4 to 15 °C transition. The 4 to 15 °C transition did not reach completion within our 100-hour measurement window (Supplementary Fig. 1). Importantly, Bpa oligomerization is reversible with respect to temperature, and the disassembly upon cooling from 37 to 4 °C proceeds at a rate of 0.23 ± 0.03 h^{-1}, consistent with a dynamic equilibrium (Supplementary Fig. 1).

To determine the absolute molecular weights of the Bpa oligomeric states, we used size exclusion chromatography coupled to multi-angle light scattering (SEC-MALS). The high-molecular weight species (P1) corresponded to the expected 228 kDa-dodecameric Bpa complex (Supplementary Fig. 2). The lower-molecular weight species eluting at ~18 mL exhibited a broad asymmetric peak indicative of oligomeric heterogeneity, precluding accurate molecular weight determination by MALS (Supplementary Fig. 2).

We used native electrospray ionization mass spectrometry (native MS) to monitor the Bpa assembly process. We first used a quadrupole time-of-flight (Q-TOF) mass spectrometer

equipped with a nano-electrospray source to determine the exact molecular weights of all species. Bpa samples were buffer-exchanged into 100 mM ammonium acetate and 20 mM 2,2-difluoroethylamine (DFEA)[22], incubated at 4 °C for 24 hours, then transferred to 37 °C to trigger assembly. Aliquots were subsequently taken at defined time points for native MS measurement (Supplementary Table 1). The native mass spectra display three sets of charge state distributions corresponding to dimeric, tetrameric, and dodecameric Bpa (Fig. 1g). The relative intensity of the dodecameric species increased with incubation time at 37 °C, corroborating our SEC data (Fig. 1e). To evaluate acquisition-induced drift for samples incubated at 4 °C, we divided the native MS acquisition into four equal time segments and integrated the signal for each separately. The resulting mass spectra were indistinguishable across the quartiles (Supplementary Fig. 3), indicating no measurable temperature- or pH-induced drift during acquisition. Notably, even after overnight incubation, low levels of dimeric and tetrameric species were still detected in our spectra, features absent from our SEC data (Fig. 1e). We attribute this apparent discrepancy to the enhanced transmission and detection efficiency of lower mass ions on our Q-TOF instrument[23,24].

To mitigate mass-dependent detection bias and to accurately identify the final distribution of oligomeric states, we turned to charge detection mass spectrometry (CD-MS). We used a prototype CD-MS instrument equipped with an electrostatic linear ion trap (ELIT) developed by the Waters Corporation. CD-MS measures the charge (z) and mass-to-charge ratio (m/z) of individual ions as they oscillate within an ELIT device. By directly detecting the image current produced by each ion, CD-MS overcomes the limitations of conventional MS for analyzing highly heterogeneous or high-mass ions, where charge state resolution is often compromised. This single-ion approach enables accurate mass determination of large noncovalent complexes regardless of peak overlap or mass distribution complexity. We analyzed Bpa samples incubated

at 37 °C with an ion trapping time of 100 ms. The resulting two-dimensional mass versus charge and one-dimensional mass histograms displayed a single dominant population corresponding to fully assembled dodecameric Bpa, with negligible signal from smaller oligomers (Fig. 1h). The absence of signal from dimers and tetramers, even under low ion trapping conditions that favour detection of small analytes, independently verifies our SEC measurements that Bpa fully assembles into dodecamers upon incubation at 37 °C.

H/D exchange mass spectrometry probes the oligomerization interface of Bpa

We used pulsed hydrogen/deuterium exchange mass spectrometry (HDX-MS) to define the structural interfaces that mediate the oligomerization of Bpa. HDX-MS is a powerful technique for probing conformational dynamics and protein-protein interactions in solution[25,26]. HDX is governed by the rate at which backbone amide hydrogens exchange with deuterium in a D_2O-based buffer, a process modulated by solvent accessibility and hydrogen bonding networks[26,27]. Regions buried within oligomerization interfaces or those stabilized by secondary structure exhibit slower deuterium uptake, whereas dynamic or solvent-exposed segments exchange more rapidly[28]. Importantly, conformational changes during assembly can either lead to an increase or a decrease in HDX rates, depending on the structural rearrangements involved[29,30]. Localization of these changes is achieved by proteolytic digestion under conditions that minimize back-exchange, followed by LC-MS analysis of deuterated peptides[31–33].

We performed time-resolved pulsed HDX-MS to monitor changes in Bpa assembly in a spatially-resolved manner. Samples of unassembled full-length WT Bpa (maintained at 4 °C) were incubated at 37 °C to initiate assembly. At defined time points, aliquots were removed and pulsed with D_2O (pH_{corr} 7.0) for 10 seconds. These samples were next quenched to stop

deuterium incorporation, and were flash-frozen and stored at -80 °C until LC-MS analysis. Our HDX-MS workflow yielded 87 peptides with quantifiable deuterium incorporation, covering 100% of the Bpa sequence with an average peptide redundancy level of 5.60 (Supplementary Fig. 4, Supplementary Table 2). The raw unprocessed spectra exhibited a mixture of unimodal and bimodal isotopic distributions, consistent with a heterogeneous conformational ensemble[34].

As a starting point for interpreting our HDX-MS data, we computed differential deuterium uptake at each time point relative to the unassembled state and visualized these differences using a heat map (Fig. 2a). We also colour-coded the available structure of dodecameric Bpa using this heat map (Figs. 2b, c)[35]. This analysis revealed substantial shifts in deuterium uptake as a function of assembly time. Regions known to participate in the canonical dodecamer subunit interface, including helix H1, exhibited progressively reduced deuterium incorporation upon incubation at 37 °C, consistent with the burial of these surfaces during oligomerization. For example, peptides 40-53, 61-85, and 98-116, spanning major portions of H1, H2, and H4, respectively, showed marked protection from exchange over time (Figs. 2b, c), indicative of decreased solvent accessibility and reinforced hydrogen bonding due to subunit packing relative to the dimeric and tetrameric structures that predominate at t = 0 (Figs. 1e, g). In contrast, residues located in the flexible C-terminal H4 region displayed increased deuterium uptake upon dodecamer formation. We interpret this increase as evidence of disengagement from interactions that stabilize lower-order oligomers. This interpretation is consistent with expectations based on a previously-determined crystal structure (PDB: 5IEU) of a truncated Bpa variant (44-153) that revealed a tetramer stabilized by inter-subunit H4-H4' interactions (Supplementary Figs. 5a, c)[12] that would protect backbone amides in these helical regions from exchange with solvent (Supplementary Fig. 6). Notably, this interface is distinct from the subunit packing observed within the context of the dodecameric Bpa assembly where H1-H4',H2-H4',

and H2-H3' closely interact (Supplementary Figs. 5b, d). Our data, thus, indicate that as the temperature increases the oligomerization equilibrium shifts toward dodecamer formation, H4 disengages from tetramer-specific interfaces, so that this region becomes increasingly solvent-exposed and exchange-competent (Figs. 2b, c).

To further dissect the kinetics of Bpa temperature-induced assembly, we selected peptides exhibiting clear bimodal isotopic distributions. Bimodality is consistent with two slowly interconverting states but can also arise from EX1 kinetics. In our data, persistence of two distributions with time-dependent population changes, consistency across multiple overlapping peptides, and our SEC-based data favour the two-state interpretation. We quantified the relative populations of protected (closed – red traces) and exposed (open – green traces) conformations at each incubation time point by fitting a pair of Gaussian functions to the obtained profiles (Fig. 3a). We modelled the time-dependent changes in the fractional population of each conformation using a first-order exponential model for all peptides displaying bimodality (Fig. 3b). This analysis yielded spatially-resolved estimates of the interconversion rate constant (k_{HDX}) (Fig. 3c). Across all peptides analyzed, k_{HDX} values averaged 0.23 ± 0.06 h^{-1}, in agreement with the oligomerization rate determined using SEC (Fig. 1f, Fig. 3c, grey bar). Together, these data define the structural and kinetic features that govern Bpa self-assembly and demonstrate that formation of the dodecamer requires dissociation of cold-stabilized lower-order intermediates that adopt a distinct packing interface.

Characterization of WT Bpa assembly using methyl-TROSY NMR

In order to examine how temperature affects the structure and oligomerization of Bpa, we turned to NMR experiments, exploiting a methyl-transverse relaxation optimized spectroscopy

(TROSY)[36] effect that enhances spectral sensitivity and resolution for large proteins[36–38]. Methyl-TROSY is particularly effective when paired with selective isotopic labelling of methyl groups ($^{13}CH_3$) from Ile, Leu, Val, and Met residues in an otherwise uniformly deuterated ([U-^{2}H]) molecule to produce [U-^{2}H; Ileδ1-$^{13}CH_3$; Leu,Val-$^{13}CH_3$/$^{12}CD_3$; Met-$^{13}CH_3$]-labeled protein, where only one isopropyl methyl group of Leu and Val is $^{13}CH_3$ labeled in a non-stereospecific manner; hereafter referred to as ILVM-labelling[39]. We recorded ^{1}H-^{13}C heteronuclear multiple-quantum coherence (HMQC) spectra that benefit from the methyl-TROSY effect[36] to monitor the temperature-dependent structural changes of Bpa. We obtained high-quality ^{1}H-^{13}C HMQC spectra at 40 °C and 18.8 T for ILVM-labeled WT Bpa samples that were preincubated at either 4 or 40 °C (Fig. 4a, multi-contour peaks). Prolonged incubation at 40 °C led to the emergence of a distinct set of peaks compared to those obtained from preincubating Bpa at 4 °C, resulting from structural changes to Bpa (Fig. 4a) and corresponding to separate conformers at low and high temperatures. Moreover, the time dependence of the interconversion was slow on the NMR chemical shift timescale as separate peaks were observed for both species at intermediate temperatures.

To monitor the kinetics and the nature of the oligomeric states involved in this interconversion, we recorded ^{1}H-^{13}C HMQC spectra over a 48-hour time course, starting from a sample pre-incubated at 4 °C for one week (t = 0; Supplementary Fig. 7). Spectra were acquired every 19 minutes so that the evolution of peak intensities could be quantified rigorously over the period of conversion. For well-resolved peaks, we tracked the time course of NMR signals unique to each of the two oligomeric species and fit the data using a first-order exponential model, yielding an interconversion rate k_{NMR} of 0.18 ± 0.01 h^{-1} at 40 °C (Fig. 4b) that agrees well with interconversion rates of 0.35 ± 0.06 h^{-1} and 0.23 ± 0.06 h^{-1} both measured at 37 °C using the SEC (Fig. 1f) and HDX-MS (Fig. 3c) approaches, respectively. To better understand the

nature of the oligomeric states involved in this interconversion, we recorded ^{1}H-^{13}C HMQC-based pulsed-field gradient diffusion experiments focusing on the methionine region over a 48-hour time course during which Bpa was incubated at 40 °C starting from 4 °C at t = 0, to infer the size of each species. The resulting diffusion coefficients were 42.2 ± 0.3 $\mu m^2 s^{-1}$ for the larger oligomeric species of Bpa present at the end of the incubation period and 58.8 ± 0.3 $\mu m^2 s^{-1}$ for the smaller species observed only at the beginning of the time course (Fig. 4c). Diffusion coefficients scale inversely with the cube root of molecular weight[40–42]. The cube of the ratio between the diffusion coefficients for each oligomeric state of Bpa yielded a value of 2.8 ± 0.1, consistent with the presence of dodecameric and tetrameric Bpa species, as supported by native MS and native CD-MS (Figs. 1g, h).

To simplify further NMR studies, we designed constructs where the temperature-dependent oligomerization behavior of Bpa was eliminated. AlphaFold3 (Supplementary Fig. 8) and our HDX-MS data (Supplementary Fig. 9a) indicate that the N and C termini of WT Bpa are disordered. Further, X-ray crystallography studies of Bpa demonstrated that N-terminal truncations significantly impact Bpa oligomerization[12]. For example, a Bpa construct spanning residues P44 to Q153, Bpa $_{44\text{-}153}$, which lacks the N-terminal helix H0, crystallizes as a tetramer composed of a dimer-of-dimers in which the subunits adopt packing interactions that are fundamentally distinct from those observed in the dodecameric assembly (Supplementary Fig. 5). In the dodecameric structures of Bpa[12,13,21], H0 packs between helices H2, H3, and H4, an arrangement that contrasts with the inter-subunit H4-H4 contacts observed in the tetrameric assembly[12]. Therefore, deletion of H0 results in an alternative inter-subunit H4-H4 interaction that favours the tetrameric architecture. Guided by these structures and our HDX-MS data which showed that the C-terminal region of Bpa is integral for the formation of the tetrameric species (Supplementary Fig. 6), but not for the dodecamer, we introduced N- and C-terminal truncations

to stabilize specific oligomeric states of Bpa. The methyl-TROSY NMR spectrum of Bpa $_{31\text{-}146}$ closely resembled that of Bpa $_{WT}$ incubated at 40 °C (i.e. dodecameric Bpa), while the spectrum of Bpa $_{45\text{-}153}$ was similar to that of Bpa $_{WT}$ incubated at 4 °C (i.e. tetrameric Bpa) (Fig. 4a). Thus, exclusion of H0 and most of the C terminal residues involved in tetramer formation (i.e., the Bpa $_{31\text{-}146}$ construct) shifts the oligomeric equilibrium toward the dodecamer, independent of temperature. Therefore, we selected the Bpa $_{31\text{-}146}$ construct, which forms a stable dodecameric structure (Supplementary Fig. 9b), for all subsequent NMR-based experiments.

The DNA binding domain of human hTRF1 is a model substrate of Bpa-20S CP

Although HspR is the only well-characterized natural substrate of Bpa, its poor solubility and lack of stability in isolation[2,11] have hindered detailed structural investigations. Our attempts to study the Bpa-HspR interaction using NMR spectroscopy were unsuccessful due to HspR's limited stability and the prolonged NMR acquisition times required. Coexpression of Bpa and HspR mitigates some of these issues but precludes titration-based assays and selective isotopic labelling of each protein for NMR-based measurements. To overcome these constraints, we sought to identify a model substrate that would be amenable for probing Bpa-substrate interactions. We focused on the DNA-binding domain of human Telomeric Repeat-binding Factor 1, a 53-residue fragment (residues 378-430 of the full-length protein, referred to hereafter as hTRF1, with residue numbering starting at 1 for this construct) that adopts a well-defined three-helix bundle fold with an unfolded fractional population of ~1% at 35 °C (PDB: 1BA5)[43,44]. hTRF1 is a well-established model system for NMR-based studies of client-chaperone interactions[44–49]. Notably, both HspR and hTRF1 employ HTH DNA-binding domains. hTRF1 is also a known client of the Hsp70 chaperone DnaK, which likewise engages HspR[16,44–47].

As in previous work[50], we independently expressed and purified the α- and β-subunits of *Mtb* 20S CP, which were subsequently reconstituted *in vitro*. We also heterologously expressed and purified WT *Mtb* Bpa and hTRF1 and demonstrated using a protease assay that hTRF1 is efficiently degraded in the presence of both WT Bpa and WT 20S CP (Supplementary Fig. 10). The 20S CP alone as well as Bpa alone, each incubated with hTRF1 showed no detectable hTRF1 degradation over the assay window (Supplementary Fig. 11). A Bpa variant with a Y173A substitution within the C-terminal GQYL motif together with WT *Mtb* 20S CP failed to support hTRF1 degradation (Supplementary Fig. 12). Similarly, hTRF1 was not degraded when WT Bpa was paired with a catalytically inactive 20S CP variant (βT1A) (Supplementary Fig. 13). These results establish that hTRF1 degradation is dependent on both Bpa and a functional 20S CP.

NMR mapping and quantification of the Bpa-hTRF1 interaction

We fully assigned the Met (3 residues; Fig. 5a), Ile (6 residues Fig. 5b), and Leu/Val (17 Leu and 5 Val residues Fig. 5c) regions of a 2D ^{1}H-^{13}C HMQC spectrum of ILVM-labeled Bpa $_{31\text{-}146}$ recorded at 40 °C and 18.8 T. Stereospecific assignments for Leu and Val methyl groups were not obtained. The spectrum of ILVM-labelled Bpa $_{31\text{-}146}$ is of excellent quality, characterized by numerous well-resolved and isolated peaks.s We sought to map the Bpa residues responsible for binding hTRF1. Upon the addition of [U-^{2}H] hTRF1 to ILVM-labelled Bpa $_{31\text{-}146}$, new peaks appeared for residues near the N terminus of helix H1 and the C terminus of H4 (Figs. 5a-c, light and dark purple contours). Both of these regions are positioned near the base of the Bpa ring[12,13,21] and precede its unstructured C terminus (e.g., V41, V47, M48, L97, L129, I133, L137, M142) (Fig. 5d). Residues showing chemical shift perturbations (CSPs) clustered into two main regions that are consistent with sites of interaction: (1) the tightly-packed interface between

adjacent Bpa subunits (I50, L93, L97, L100, L129), and (2) the more solvent-exposed lower ring (V41, V47, M48, I133, L137, M142). The solvent-exposed residues form hydrophobic bands within the interior of the ring structure and are accessible for possible substrate engagement (Fig. 5d, Supplementary Fig. 14). The inner ring displays a negatively-charged patch located near the middle of H4 (e.g., E127) and a positively-charged patch at the C terminus of H4 (e.g., R145) (Fig. 5d, Supplementary Fig. 14). These areas are proximal to V47, M48, L129, and M142, that showed CSPs, suggesting that electrostatic interactions also contribute to hTRF1 recognition, consistent with the findings of von Rosen et al. which implicate these same residues in binding[2,21]. Notably, the hydrophobic residues at the C-terminal portion of helix H4 that exhibit CSPs and are accessible for substrate binding in the dodecameric Bpa are either fully or partially buried at the inter-subunit interface in the tetrameric construct (Supplementary Fig. 15), suggesting that their accessibility is regulated by the Bpa oligomerization state.

To quantify the strength of the Bpa-hTRF1 interaction we performed NMR titrations using [U-^{2}H] hTRF1 and ILVM-labelled Bpa $_{31\text{-}146}$ at a pair of salt concentrations (50 mM or 300 mM KCl) to evaluate the effects of ionic strength on the association (Figs. 5e-g). For experiments performed at 50 mM KCl, we found that the addition of equimolar amounts of hTRF1 to Bpa $_{31\text{-}146}$ (subunit concentration) led to the formation of visible protein aggregates and, concomitantly, an increase in solution turbidity. Therefore, we reduced the hTRF1 concentration by 10-fold and worked at a [Bpa $_{31\text{-}146}$]:[hTRF1] ratio of 10:1, starting at concentrations of 900 μM (subunit concentration) and 90 μM for Bpa $_{31\text{-}146}$ and hTRF1, respectively, and then serially diluted the mixture and recorded ^{1}H-^{13}C HMQC spectra, tracking changes in the ^{1}H or ^{13}C chemical shifts (Fig. 5e). In contrast, at 300 mM KCl there was no evidence of protein aggregation or solution turbidity, and a standard titration was performed where [Bpa $_{31\text{-}146}$] was kept constant at 100 μM (subunit concentration) with [hTRF1] varied (Fig. 5f). For residues exhibiting clear peak

displacements as a function of added hTRF1 (Figs. 5e-g), the data were fit to a model assuming exchange kinetics (hTRF1 on/off) that are fast on the NMR chemical shift timescale to extract binding affinities and stoichiometries. Notably, fits of Carr-Purcell-Meiboom-Gill (CPMG) relaxation dispersion profiles recorded with a salt concentration of 50 mM and with several different concentration ratios of Bpa $_{31\text{-}146}$ and hTRF1 to a two-site exchange model (interconversion between Bpa $_{31\text{-}146}$ free and bound with hTRF1) indicate exchange rates greater than 1500 s^{-1} (Supplementary Fig. 16). The rates obtained are significantly larger than differences in ^{13}C chemical shifts between free and bound Bpa $_{31\text{-}146}$ (Fig. 5e), validating the assumption of fast exchange. We further assumed that hTRF1 binds to Bpa only when unfolded, as the ^{1}H-^{13}C HMQC spectrum of ILVM-labelled hTRF1 in the bound form clearly indicates an unfolded ligand (Supplementary Fig. 17). The equilibrium constants for the hTRF1 folding/unfolding reaction (in the absence of Bpa) at 50 mM and 300 mM KCl, that are also required for our analyses, were established by recording chemical exchange saturation transfer (CEST) experiments[51] (Supplementary Fig. 18), which yielded unfolded hTRF1 fractions of ~0.14 and ~0.07, respectively.

The titration data were fit to a model in which dodecameric Bpa successively binds *n* copies of hTRF1, independent of salt concentration, with a distinct global microscopic dissociation constant at each [KCl] value (see Supplementary Methods). Using unfolded hTRF1 fractions indicated above, we estimated dissociation constants K_d for the Bpa $_{31\text{-}146}$-hTRF1 complex of < 0.2 μM at 50 mM KCl (Supplementary Fig. 19a) and 1.5 ± 0.2 μM at 300 mM KCl (Supplementary Fig. 19b). A plot of reduced-χ^2 versus *n* exhibited a well-defined global minimum with a binding stoichiometry of three hTRF1 molecules per Bpa $_{31\text{-}146}$ dodecamer (Supplementary Fig. 19c). Notably, when it is assumed that hTRF1 can bind equally well to Bpa $_{31\text{-}146}$ as an unfolded or folded substrate an identical *n* value is obtained, with approximately ten-

fold higher K_d values at each salt concentration. Together, these experiments identify the hTRF1 binding interface on Bpa, quantify the model-dependent interaction strength as a function of ionic strength, and establish the stoichiometry of the hTRF1-Bpa $_{31\text{-}146}$ complex.

Disordered substrate recognition is mediated by hydrophobic patches on hTRF1

The identification of the Bpa-binding interface on hTRF1 is complicated by the fact that hTRF1 unfolding and binding are coupled, as the free form of the ligand (i.e. hTRF1) is predominantly folded (see above; Supplementary Fig.16), while the bound form is not. To this end, we generated a panel of [U-^{15}N] hTRF1 deletion variants that lack the ability to adopt a structured fold. We recorded ^{1}H-^{15}N HSQC spectra of the variants in the absence and presence of 10-fold monomer equivalents of Bpa $_{31\text{-}146}$ at 300 mM KCl and 40 ^{o}C (Fig. 6a). We obtained high-quality datasets characterized by well-resolved resonances focused on a narrow ^{1}H chemical shift window that is expected for unfolded proteins. We obtained complete backbone assignments for the hTRF1 fragments under these conditions (Fig. 6a). Upon titration with Bpa $_{31\text{-}146}$, we measured a marked reduction in signal intensities for a subset of hTRF1 amide resonances (Figs. 6a, b). The attenuated cross-peaks map to two distinct sequence segments: residues ^{6}WLW^{8} and ^{30}ILL^{32}, corresponding to a pair of hydrophobic segments (Fig. 6b) previously identified as functionally relevant in hTRF1-DnaK (client-chaperone) interactions[44]. The selective disappearance of peaks results from extensive line broadening caused by two factors: an increase in the effective rotational correlation time of hTRF1 upon binding to the 155 kDa Bpa $_{31\text{-}146}$ particle, and enhanced transverse relaxation due to the proximity of hTRF1 amide probes to protons from Bpa. In this case, Bpa $_{31\text{-}146}$ was fully protonated, which promotes more efficient

relaxation than would be observed with a perdeuterated binding partner. Regions of hTRF1 that are no longer visible in HSQC spectra thus correspond to interaction sites with the Bpa client.

The hTRF1 deletion variants can also be used to assess whether the affected residues function as independent or cooperative binding elements. Removal of residues ^{30}ILL^{32} (e.g., Δ20-38, Δ20-53, Δ20-38, Δ41-43) failed to eliminate binding near ^{6}WLW^{8}, suggesting that the two sites act independently. In contrast, deletion of ^{6}WLW^{8} abrogated all line broadening effects in the N-terminal region, suggesting its essential role in regulating N-terminal substrate contacts with Bpa $_{31\text{-}146}$. Sequence analysis reveals that both ^{6}WLW^{8} and ^{30}ILL^{32} are the most hydrophobic segments of the construct (Fig. 6b – grey trace) and are flanked by polar and charged residues. While the exact ^{6}WLW^{8} and ^{30}ILL^{32} motifs are not present in HspR, short hydrophobic segments flanked by polar/charged residues, the same pattern we highlight in hTRF1, are evident in both the HTH domain and the disordered C-terminal region of HspR (Supplementary Fig. 20). These residues have been proposed to facilitate substrate pre-orientation via electrostatic steering, followed by hydrophobic engagement at the proteasomal binding interface[2]. Notably, structurally diverse proteins (e.g., FynSH3, drkNSH3, Im7, α-synuclein) that span a broad range of isoelectric points (Supplementary Fig. 21) did not interact with Bpa $_{31\text{-}146}$ as measured by NMR (Supplementary Fig. 22), underscoring the sequence-encoded specificity of the Bpa-hTRF1 interaction. Overall, our findings establish Bpa as a selective reader of short hydrophobic motifs embedded within disordered regions, hallmarks of proteasomal substrates.

Discussion

Prior cellular, biochemical, and structural studies have established the importance of Bpa within the *Mtb* proteasome system[2,6,7,11–15,21], yet the structural heterogeneity of Bpa and the mechanisms governing its substrate recognition have are incompletely understood. Here, we combine native MS, HDX-MS, and methyl-TROSY NMR spectroscopy, approaches not previously applied to Bpa, with a tractable model substrate to address these knowledge gaps. We show that Bpa exists in a temperature-sensitive equilibrium between dimers, tetramers and dodecamers, and only the fully assembled dodecamer is competent for substrate recognition and delivery to the 20S core particle. HDX-MS, native MS, and CD-MS reveal a cold-stabilized tetrameric species whose HDX protection pattern, particularly at helix H4, is consistent with the inter-subunit packing observed in crystallographic studies of a truncated Bpa variant identified as a cold-stabilized tetrameric state[12]. These H4-H4' interactions must be disrupted to permit formation of the functional dodecamer. We further establish hTRF1 as a structurally tractable model substrate of Bpa and use it to elucidate interactions that are key for substrate engagement. Our experiments exploiting methyl-TROSY NMR establish that Bpa $_{31\text{-}146}$ recognizes two solvent-exposed hydrophobic surfaces on hTRF1, ^{6}WLW^{8} and ^{30}ILL^{32}, which are flanked by polar residues. These motifs interact with two distinct regions on Bpa $_{31\text{-}146}$: a hydrophobic lower-ring surface and a charged interior pocket, revealing a bipartite binding mechanism. Quantitative NMR titrations show that Bpa $_{31\text{-}146}$ binds up to three hTRF1 molecules per dodecamer with micromolar affinity, modulated by salt concentration, further supporting the relevance of electrostatics. We note that assessing the generality of the mechanism presented here is difficult because HspR remains the only natural Bpa substrate characterized in detail. Because hTRF1 is an unnatural substrate, we present these features as principles suggested by a model client. Whether analogous hydrophobic motifs and stoichiometry govern recognition of natural substrates (e.g., HspR) remains to be tested.

Collectively, our *in vitro* findings support a model in which temperature acts as a switch for Bpa activity. It is to be established if this model is applicable *in vivo*. Although the host core temperatures remain relatively constant at 37 ºC, *M. tuberculosis* experiences a dramatic shift in proteostatic stress when transitioning from environmental persistence to the intracellular environment of the host[5]. *Mtb* can survive for hours in aerosols and for weeks to months on surfaces[52] where metabolic activity is minimal and proteostatic demands are low. Elevated temperatures, such as those encountered during phagocytosis by the host macrophages, may drive dodecamer formation, thereby enabling recruitment and degradation of substrates like HspR, a key transcriptional repressor of heat shock genes (*dnaK, gprE, dnaJ, hspR*)[2]. We speculate that Bpa may function as part of a broader stress-sensing mechanism that leads to proteasomal activation and transcriptional reprogramming in response to changing conditions. However, this model remains to be validated in a cellular context, and future experiments using Bpa variants locked in defined oligomeric states will be essential to assess the physiological relevance of temperature-dependent assembly. Small molecules that trap WT Bpa in its tetrameric state and prevent functional dodecamer formation may offer a novel strategy for disrupting the *Mtb* proteasome system.

By establishing the structural heterogeneity of Bpa and revealing how it engages substrates via discrete hydrophobic motifs, our work lays the foundation for understanding proteasomal selectivity in *M. tuberculosis*. The tools and constructs developed here provide a blueprint for dissecting regulated proteolysis in bacterial systems. More broadly, the thermosensitive structural transition described here may represent a general strategy by which bacteria couple protease activation to environmental change.

Methods

Plasmids and constructs

Codon-optimized genes encoding for *M. tuberculosis* full-length wild-type Bpa (UniProt: *bpa*, P9WKX3), proteasome α-subunit (UniProt: *prcA*, P9WHU1), and proteasome β-subunit excluding the propeptide (UniProt: *prcB*, P9WHT9) were synthesized and inserted into kanamycin-resistant pET24-based vectors (Biobasic, Markham, ON, Canada). All constructs include a N-terminal His_6-SUMO affinity tag, excluding the β-subunit which has a C-terminal TEV-SUMO-His_6 tag. Point mutations were introduced via the QuikChange method[53]. The DNA binding domain of hTRF1 (residues 378-430 of the full-length protein, Uniprot: P54274) was used as the unnatural substrate of Bpa for NMR experiments. Additionally, truncated hTRF1 constructs were used to probe regions of the substrate implicated in Bpa binding (Δ6-8; Δ20-38, Δ20-38, Δ20-38; Δ41-43, Δ20-38; Δ47, Δ39-53). All hTRF1 constructs include a N-terminal His_6-SUMO affinity tag.

Protein expression and purification

Multiple Bpa constructs (WT, Y173A, 31-146, 45-153), hTRF1 and its truncated variants, proteasome α-subunit, and proteasome β-subunit were expressed and purified. Plasmids were transformed into chemically competent NEB BL21 T7 Express *LysY E. coli* cells. Different growth media were used depending on the type of desired isotope labeling. For the production of natural abundance proteins, cells were grown in lysogeny broth (LB) to an OD_{600} of 0.6-0.8 before induction with 0.2 mM isopropyl β-d-1-thiogalactopyranoside (IPTG). For the production of uniform ^{15}N-labeled proteins, cells were grown in M9 minimal media, prepared using H_2O milli-Q, with $^{15}NH_4Cl$ as the sole nitrogen source. For the production of perdeuterated proteins, cells

were grown in M9 minimal media, prepared using 99% D_2O, with d_7 glucose as the sole carbon source and, in the case of ILVM labeling, the following precursors were added 1 h before the induction of protein overexpression: 100 mg/L [ε-13C]-methionine (CLM-206-PK; Cambridge Isotope Laboratories), 60 mg/L α-ketobutyric acid (CDLM-7318; Cambridge Isotope Laboratories), and 100 mg/L α-ketoisovaleric acid (CDLM-7317; Cambridge Isotope Laboratories)[54].

All Bpa constructs and 20S CP subunits were expressed overnight at 16 °C while shaking at 180 rpm. Cells were harvested via centrifugation at 5,000 × *g* for 20 minutes for all proteins. Cell pellets were frozen at -20 °C until future purification. All cells were resuspended in 30 mL of lysis buffer (see below) and lysed via sonication (Heat Systems INC Sonicator XL 2020 Ultrasonic Liquid Processor) using a 5-minute program consisting of 10 seconds on and 20 seconds off. Ion metal affinity chromatography (IMAC) buffers for Bpa constructs consisted of 50 mM Tris, 600 mM KCl, supplemented with either 20 (lysis/wash), 50 (strong wash), or 500 (elution) mM imidazole at pH 7.0. The 20S CP IMAC buffers consisted of 50 mM Tris, 300 mM NaCl, supplemented with either 20 (lysis/wash), 50 (strong wash), or 500 (elution) mM imidazole at pH 7.0. Eluted proteins were dialyzed overnight in lysis buffer + 1 mM dithiothreitol (DTT) with the appropriate proteases to cleave the affinity tags. The 20S CP was assembled using the protocol described by Turner *et al.* (2025)[50]. After dialysis and tag cleavage, a second IMAC step was conducted to remove cleaved affinity tags. Size exclusion chromatography (SEC) using either a Superose 6 or Superdex 200 column was performed using an ÄKTA pure™ chromatography system as the final purification step. Purified Bpa constructs were never frozen and stored at 4 °C until further use.

hTRF1 and its truncated variants was transformed, grown, induced, and harvested as described above. hTRF1 cell pellets were resuspended in 30 mL of denaturing lysis buffer and

lysed via sonication (Heat Systems INC Sonicator XL 2020 Ultrasonic Liquid Processor) using a 5-minute program consisting of 10 seconds on and 20 seconds off. Initial IMAC was performed under denaturing conditions. Buffers consisted of 50 mM Tris, 6 M Gdn-HCl, supplemented with either 20 (lysis/wash) or 50 (strong wash) mM imidazole at pH 8.0. The elution step was conducted using a buffer containing 50 mM NaH_2PO_4, 200 mM KCl, 2 mM EDTA, and 300 mM imidazole at pH 8.0. Endpoints for the elution step were determined via Bradford assay. Eluted proteins were dialyzed overnight in 50 mM NaH_2PO_4, 200 mM KCl, 2 mM EDTA, 50 mM imidazole, and 1 mM DTT at pH 8.0 with the appropriate proteases to cleave the affinity tags. After dialysis and tag cleavage, a second IMAC step was conducted to remove the cleaved affinity tags. SEC using a Superdex 75 was performed using an ÄKTA PUR™ chromatography system as the final purification step. Purified hTRF1 was flash frozen and stored at -80 °C until further use.

Protein quality for all stages of IMAC and SEC was assessed using sodium dodecyl sulfate polyacrylamide gel electrophoresis (SDS-PAGE). Final concentrations of all protein stocks were determined spectrophotometrically using a NanoDrop 2000 spectrophotometer. All extinction coefficients for concentration measurements were calculated via ExPASy's ProtParam (https://web.expasy.org/protparam/).

Discontinuous SDS-PAGE-based protein degradation assays

Protein degradation assays were performed by incubating Bpa (WT or Y173), 20S CP (WT or T1A), and hTRF1 at 37 °C over 48 hours. Protein concentration for all reactions consisted of 0.8 μM Bpa (dodecamer concentration), 0.14 μM 20S CP, and 10 μM hTRF1. Aliquots were taken at discrete time points and the reaction was quenched by mixing the reaction mixture with

Laemlli buffer (4:1), followed by subsequent heat inactivation at ~95 °C for 5 minutes[55]. Visualization of protein degradation was performed using SDS-PAGE. 20 µL of sample was loaded and run into 20% acrylamide gels for all samples to ensure adequate visualization. BlueElf Prestained Protein Marker (5-245 kDa) as a molecular weight standard. Imaging of all gels was conducted on a BioRad ChemiDoc Imaging System (Hercules, CA).

Size exclusion chromatography – temperature-dependent oligomerization

To monitor dodecamer association, unassembled Bpa (4 °C) at 30 µM (subunit concentration) was incubated at either 15, 25, or 37 °C and sampled as a function of incubation time to probe oligomeric state. Separate protein stocks were made for each of the time points (0 , 2 ,4 , 6 , 8 , 12 , 16 , 20 , 24, and 98 h) so as to not remove the same protein stock from the incubator multiple times during the course of the experiment. Protein samples were spun down for 5 minutes at 21,130 × *g* to pellet any aggregated protein before incubation began. SEC analysis was performed using an ACQUITY UPLC Protein BEH SEC 200 Å column (1.7 µm, 4.6 mm x 150 mm, Part#: 186005225, Waters) outfitted with a MaxPeak™ Premier Protein Guard column (2.5 µm, 4.6 mm x 30 mm, Part#: 186009969, Waters) on an Agilent 1100 Series HPLC system. The running buffer composed of 50 MmM HEPES, 200 mM KCl, pH 7.0. The flow rate for all runs was 0.3 mL min^{-1}. Each injection consisted of 10 µL of a 30 µM Bpa (subunit concentration) solution, quantified by absorbance at 220 nm. Visualization and fitting of all SEC chromatograms were made using scripts written in house in Python 3.13.5. The P1, P2 and P3 species were fit using three exponentially-modified Gaussians[56]. The integrals of the peaks were then used to derive the fraction population of P1 and P2+P3. Mean population percentage values and uncertainties of P1 and P2+P3 populations were calculated via bootstrapping in which 5% of the

chromatographic data was resampled and independently fit (n=1000).s. The time dependencies of the populations were subsequently fit using a first order exponential model (Equation 1) to extract an association rate, *k*. Bootstrapping uncertainty values were used as weights during population fitting such that data points with lower variability contributed proportionally more to the fit. Final extracted *k* values are reported ± 2σ.

$$f(t) = A \cdot e^{-k \cdot t} + B \qquad \text{(Eq. 1)}$$

SEC-MALS

WT Bpa was subjected to SEC-MALS analysis to determine the molecular weight of all oligomeric species in solution as a function of incubation time at 37 °C using an OMNISEC multi-detector SEC system (Malvern Panalytical, United Kingdom) fitted with OMNISEC RESOLVE and OMNISEC REVEAL modules. 100 µL samples were injected at 2 mg/mL were loaded onto a P3000 Protein SEC column (300×8 mm, Malvern Panalytical) equilibrated in 150 mM NaCl, 50 mM Tris-HCl, pH 7.5 at a flow rate of 1 mL min^{-1}. Molecular weight was calculated using light scattering detectors at 90° (right angle light scattering) and 7° (low-angle light scattering). BSA was used as a standard for molecular weight calibration.

Pulsed hydrogen deuterium mass spectrometry (HDX-MS)

To probe the assembly of Bpa, we performed pulsed HDX-MS after incubating apo WT at 37 °C for defined time intervals. All buffers (H_2O and D_2O-based) used for pulsed HDX consisted of 50 mM imidazole, 100 mM KCl, 0.3% NaN_3 [w/v] at pH 7.0. The D_2O-based exchange buffer

consisted of the same components however the pD was adjusted to 6.6 (pH_{corr} 7.0) using the standard electrode method[57]. Unassembled Bpa (32 μM at 4°C) was incubated at 37 °C and periodically sampled before being pulse labelled in D_2O-based exchange buffer for 10 seconds. HDX was started via 40-fold dilution of protein into D_2O based exchange buffer (final Bpa monomer concentration of 0.8 μM) resulting in a 97.5% D_2O-based buffer. Exchange was quenched via 1:1 (v/v) dilution into a quench solution consisting of 250 mM NaH_2PO_4, 3 M Gdn-HCl, and 3 mM n-dodecylphosphocholine at pH 1.52 followed by immediate flash freezing in liquid N_2. Final pH after quenching of samples was determined to be 2.5. All quenched aliquots were stored at -80 °C until LC-MS.

Sample handling and reverse phase liquid chromatography was conducted using a Waters ACQUITY™ M-Class UPLC™ with HDX technology. 20 pmol of sample was digested on-line at 15 °C using a nepenthesin-2 immobilized protease column (Affipro, AP-PC777 004, 1 mm × 20 mm). The resulting peptides were trapped for 3 minutes using a BEH™ 778 C18 (1.7 μm, 2.1 mm × 5 mm; Part#: 186003975, Waters) column at a flowrate of 100 μL min^{-1}. Peptide separation was achieved on an HSS T3 (1.8 μm, 1.0 × 50 mm; Part#: 780 186003535, Waters) column. Liquid chromatography consisted of an 8-minute linear acetonitrile:H_2O gradient acidified using 0.1% [v/v] formic acid (acetonitrile ramped from 5 – 35%) at 0 °C and at a flowrate of 100 μL min^{-1}. The injection port and sample loop were cleaned between each injection to ensure minimal carryover using a solution consisting of 1.5 M Gdn-HCl, 4% (v/v) acetonitrile, 0.8% (v/v) formic acid, and 1.5 mM dodecylphosphocholine.

The LC outflow was then directed to a coupled Waters SYNAPT™ G2Si Q-TOF mass spectrometer equipped with a standard electrospray source operated in positive ion mode with a capillary voltage of +3 kV. The time-of-flight mass analyzer was set to resolution mode with ion mobility enabled and spectra were recorded over the 50 − 2000 m/z range at a scan rate of

0.4 s^{-1}. The instrument was externally calibrated using sodium iodide (700008892) over the 50 – 2000 *m/z* range. The instrument was dynamically calibrated during runs by infusing LeuEnk solution (1+, 556.2771 Th) from the LockSpray capillary every 20 seconds at a flow rate of 10 µL min^{-1}. The quadrupole was controlled manually and was set to dwell at 300 m/z for all runs.

All HDX-MS experiments were measured in technical triplicate to ensure reproducibility. Peptide mapping was conducted via ProteinLynx Global Server (v3.0.3) using data from undeuterated samples acquired during MS^E experiments performed as detailed previously[58]. Peptide filtering parameters were taken from Sorenson et al. [59]. All spectra for peptides that persisted after filtering were visually inspected to ensure only high-quality spectra were included in the final data set. Undeuterated control samples were prepared and quenched in an identical manner except for being in an H_2O-based solutions. All data analysis was conducted using DynamX v3.0 (Waters). All figures were generated using HDgraphiX[35] and ChimeraX 1.10[60].

HDX-MS isotopic envelope fitting

All HDX-MS data were analyzed in Python (v3.13.5) using NumPy, pandas, matplotlib, and the lmfit nonlinear least-squares minimization library. Spectra corresponding to individual peptides at different deuterium labeling times were imported using the Waters Data Importer module of UniDec[61] as intensity versus m/z traces. For each peptide, we fit a pair of Gaussian components to the bimodal isotopic distributions, corresponding to protected (closed) and exposed (open) conformational states. The lower m/z distribution for all spectra were denoted as “closed” and the higher m/z distribution was denoted “open”. In the first pass, spectra across all time points were fit simultaneously with minimal constraints. For each peptide, the center, amplitude, and width of each Gaussian function were allowed to vary freely within broad bounds. The purpose

of this pass was to determine a consensus set of parameters, in particular the approximate peak positions and widths, that define the isotopic envelope shape for each peptide. This step reduces user bias and ensures that the minimum number of Gaussian functions is used. Parameters from the first pass were then used as starting values for a second round of fits. In this pass, amplitudes were fully optimized for each spectrum, while centers were only allowed to vary within ±1/z of their first-pass values, and width values were allowed to vary within ±20% of the first-pass value. These constraints enforce consistency in the isotopic envelope shape across time points, while still accommodating small shifts in centroid mass and width due to increasing deuterium uptake. Ultimately, each spectrum was modeled using two Gaussian components, one for the closed state and one for the open state, whose amplitudes were independently optimized while centers and widths remained constrained. This strategy improves the robustness of the fitting parameters, prevents overfitting to noise and ensures that measured population changes directly report on protein dynamics in solution. The integral of the closed and open Gaussians were used to calculate fractional populations for each distribution. These populations were then fit using a first-order exponential model (Eq. 1) to extract an association rate *k*.

Native ESI MS – Temperature dependent oligomerization

All MS measurements for apo Bpa were performed in positive-ion mode on a Waters SYNAPT G2Si instrument equipped with a nano ESI source. The time-of-flight mass analyzer was set to resolution mode and recorded spectra over the 400-8000 *m/z* range at a scan rate of 1 s^{-1}. The quadrupole transmission profile was operated in automatic mode. All other instrument parameters are listed in Supplementary Table 1. All LC-MS grade reagents were obtained from

Fischer Scientific (Hampton, NH). LC-MS grade ammonium acetate (cat. no. 14267) and water (cat. no. w74) were used to prepare native MS buffers. Reagent grade 2,2-difluoroethylamine (DFEA) (cat. no. D4758) was obtained from TCI America (Portland, OR) and added to the ammonium acetate solution to ensure proper buffering within the capillary during native MS experiments[22]. The final pH of the ammonium acetate + DFEA was adjusted at room temperature using LC-MS grade ammonium hydroxide (60046886) and formic acid (A11750). Bpa was buffer exchanged into 100 mM ammonium acetate at pH 7.0 using a 10k molecular weight cutoff Amicon centrifugal concentrator (3 buffer exchange cycles). After buffer exchange, the protein stock (20 μM – Bpa subunit) was centrifuged and filtered using a 0.2 μm syringe filter device. After filtering, Bpa was diluted to a final concentration of 10 μM using 0.4 M ammonium acetate and 1 M DFEA at pH 7.0. The final concentrations of ammonium acetate and DFEA within the sample were 100 mM and 20 mM, respectively. The Bpa protein stock was then incubated at 37 °C overnight and periodically sampled to monitor the oligomeric state of Bpa as a function of assembly time. At discrete time points ranging from 0 – 24 h, 10 μL of Bpa was sampled and immediately loaded into a borosilicate capillary pulled to a fine tip using a P-1000 micropipette puller (Sutter Instruments). Capillary voltage was applied via a platinum wire in contact with the sample inserted through the open end of the capillary. All specific instrument parameters are listed in Supplementary Table 1. Deconvolution of data collected using the Synapt G2Si instrument was performed using UniDec[61]. All figures were generated using scripts written in house in Python 3.13.5.

Charge detection mass spectrometry

Apo Bpa was diluted into 10 mM ammonium acetate solution (Invitrogen, AM9070G) to a concentration of 20 μM (Bpa subunit). A 50 μL aliquot of apo Bpa was buffer exchanged three times with 10 mM ammonium acetate solution (400 μL each time) using Amicon ultra centrifugal filters with a 10 kDa molecular weight cut-off (Merck, UFC501008). Buffer-exchanged samples were then incubated overnight at 37 °C. The incubated samples were diluted to a final concentration of 1 μM (Bpa monomer) prior to charge detection mass spectrometry (CDMS) analysis. Mass analysis was performed using a prototype charge detection mass spectrometer with an electrostatic linear ion trap (ELIT), based on the instrument architecture designed by the Jarrold group at Indiana University, which has been described previously[62]. 5 μL of each sample was loaded into separate glass emitters (5 μm internal diameter) and ions were generated by positive-ion-mode static nanoelectrospray ionization (nanoESI) using a home-built source. Ions were trapped in the ELIT for 100 ms and the frequency and amplitude information were converted to m/z and z values, respectively, and ultimately mass (m/z × z). These data were subsequently binned to generate the corresponding spectra (histograms). The spectra were collected until a minimum of approximately 5000 ions were recorded within the mass range of 0-1 MDa. Signal processing and data visualization were performed using software developed in-house. Visualization of CDMS data was performed using in house scripts in Python 3.12.4.

Nuclear magnetic resonance (NMR) spectroscopy

All NMR experiments were recorded using one of the following spectrometers: Bruker AVANCE III HD 14.1 T, Varian INOVA 14.1 T, or Bruker AVANCE III HD 18.8 T, all equipped with cryogenically-cooled, triple-resonance probes. All datasets were processed with the NMRPipe

software package[63]. ^{1}H-^{13}C HMQC[14] and ^{1}H-^{15}N HSQC spectra were recorded using standard pulse schemes[64].

Diffusion experiments for Bpa were recorded using a previously-published pulse sequence[65] that generates ^{15}N-edited spectra; in the present case where ^{13}C-edited spectra are recorded, ^{15}N pulses are replaced by ^{13}C pulses. Dephasing and rephasing pulsed-field gradients are applied as bipolar pairs along the y-axis to minimize the effect of convection, with each pair of duration 3 ms, and strengths up to 0.26 T/m. The diffusion delay was set to 0.3 s.

The assignment of methyl groups in $Bpa_{31\text{-}146}$ was initially carried out by site-directed mutagenesis where leucine or valine residues were singularly replaced by an isoleucine, and isoleucine or methionine residues were singularly replaced by a leucine. This strategy led to the identification of those assignments labeled in black in Figure 5a-c. All other assignments, labeled in grey, were obtained using three types of NOESY experiments: 1) 3D HMQC-NOESY ($^{1}H[t_1]$ → $^{13}C[t_2]$ → mixing time → $^{1}H[t_3]$) with a mixing time of 250 ms, recording 40 and 72 complex increments, respectively, for the ^{1}H ($t_{1,max}$ = 17.9 ms) and ^{13}C ($t_{2,max}$ = 19.9 ms) indirect dimensions, for a total duration of 48 hours; 2) 3D F_1-^{13}C, F_2-^{13}C HMQC-NOESY-HMQC ($^{13}C[t_1]$ → mixing time → $^{13}C[t_2]$ → $^{1}H[t_3]$) with a mixing time of 50 ms, recording 66 complex increments for both indirect dimensions ($t_{1,2max}$ = 18.2 ms), for a total duration of 33 hours; 3) a second 3D F_1-^{13}C, F_2-^{13}C HMQC-NOESY-HMQC with a mixing time of 250 ms, recording 72 complex increments for both indirect dimensions ($t_{1,2max}$ = 19.9 ms), for a total duration of 44 hours.

Methyl ^{13}C CEST experiments were recorded for hTRF1 at [KCl] of 50 mM and 300 mM using the DANTE selective saturation scheme[66,67]. A pair of experiments with ^{13}C weak B_1 fields fields of 10 and 20 Hz were acquired for each sample, while the position of the B_1 field was swept in 41 increments over the spectral window of the DANTE scheme (4 ppm).

Methyl CPMG experiments were acquired for ILVM labeled Bpa_{31-146} in the presence of perdeuterated hTRF1 using the TROSY CPMG pulse sequence[68]. The relaxation of the TROSY component of the {^{13}C,^{1}H} multiple quantum coherence was measured during a fixed CPMG delay of 20 ms with the application of a variable number of ^{13}C refocussing pulses (field strength of 17.2 kHz) with ν_{CPMG} values ranging from 50 Hz to 2 kHz (14 values plus 3 duplicates). The non-TROSY rapidly decaying components of the {^{13}C,^{1}H} multiple quantum coherence were suppressed by applying a purge element prior to the CPMG period, as previously described[68].

Titration of the Bpa-hTRF1 interaction by NMR

As described in the text, two different titration series were recorded, one at 50 mM KCl and the other at 300 mM KCl to evaluate the role of electrostatics in the Bpa-hTRF1 interaction. Experiments at low [KCl] were recorded using a Bpa monomer:hTRF1 ratio of 10:1, with starting [Bpa] and [hTRF1] of 900 µM (subunit concentration) and 90 µM, respectively. ^{1}H-^{13}C HMQC experiments were recorded for successive dilutions of this sample ([Bpa subunit] = {900 µM, 400 µM, 100 µM, 50 µM, 25 µM} = [hTRF1] × 10), as well as for the reference sample with Bpa alone. A second titration series was recorded for the 300 mM KCl sample using a standard titration where [Bpa] was kept constant at 100 µM (subunit concentration) and [hTRF1] was varied ({0 µM, 10 µM, 25 µM, 50 µM, 100 µM, 150 µM}).

Profiles of chemical shift changes from the two titration series were fit together to a model in which dodecameric Bpa successively binds single copies of unfolded hTRF1 until *n* copies are bound, with a constant global microscopic dissociation constant K_d (i.e., no cooperativity) for each binding event:

$$B_{12}T^{u}_{i-1} + T^{u} \rightleftarrows B_{12}T^{u}_{i} \quad , K^{i}_{eq} = K_D \cdot i/(n-i+1). \qquad \text{(Eq. 2)}$$

In Eq. 2, subscript *i* indicates the number of bound hTRF1 molecules with 1 ≤ *i* < *n*, B_{12} and $B_{12}T_i^u$ denote the dodecameric Bpa species and the Bpa dodecamer-hTRF1 complex comprised of *i* copies of the unfolded form of hTRF1, respectively, and T^u denotes the unfolded hTRF1 ligand. The folding/unfolding equilibrium of hTRF1 is given by

$$T^f \rightleftarrows T^u, \qquad \text{(Eq. 3)}$$

where $T^u/(T^f+T^u) = f^u$ is 0.14 and 0.07 at 50 mM and 300 mM KCl, respectively, as established by CEST measurements of isolated hTRF1 under conditions that are identical to those used for the titrations.

Note that in Eq. (2) the equilibrium constants for each binding event, K^i_{eq}, are related to the factor $i/(n-i+1)$ that accounts for the multiplicity of ways in which ligand can be added to $B_{12}T_{i-1}^u$ $(n-i+1)$ and subtracted from $B_{12}T_i^u$ (i). Profiles at both [KCl] were fit together using Eqs. 2 and 3, with *n* treated as a global parameter, i.e. assumed to be salt-independent, while separate dissociation constant K_d values are fit, one for each [KCl].

In the above analysis it is assumed that Bpa can only bind to unfolded hTRF1 (T^u). Alternatively, if Bpa binds to both folded (T^f) and unfolded hTRF1 with the same affinity, the same best-fit value of *n* = 3 is obtained, however the K_d values increase by *ca.* one order of magnitude. Thus, while the K_d values are model dependent, the value of *n* is less sensitive to the mechanism of binding.

Data availability

Mass spectrometry data are available from the MassIVE database as entry MSV000099239 (https://massive.ucsd.edu/ProteoSAFe/dataset.jsp?task=1e313073db3545efaf0ba91f95fa9a72) (HDX raw data).

Code availability

The code used for SEC, HDX, and NMR analysis in this study have been deposited in the Zenodo database under accession code [https://zenodo.org/records/18498816] (Code deposition).

References

1. Darwin, K. H., Ehrt, S., Gutierrez-Ramos, J.-C., Weich, N. & Nathan, C. F. The proteasome of Mycobacterium tuberculosis is required for resistance to nitric oxide. *Science* **302**, 1963–1966 (2003).
2. von Rosen, T., Pepelnjak, M., Quast, J.-P., Picotti, P. & Weber-Ban, E. ATP-independent substrate recruitment to proteasomal degradation in mycobacteria. *Life Science Alliance* **6**, (2023).
3. Janssen, G. V. *et al.* Development of Tyrphostin Analogues to Study Inhibition of the Mycobacterium tuberculosis Pup Proteasome System. *ChemBioChem* **22**, 3082–3089 (2021).
4. Lin, G., Tsu, C., Dick, L., Zhou, X. K. & Nathan, C. Distinct Specificities of Mycobacterium tuberculosis and Mammalian Proteasomes for N-Acetyl Tripeptide Substrates. *J Biol Chem* **283**, 34423–34431 (2008).
5. Lupoli, T. J., Vaubourgeix, J., Burns-Huang, K. & Gold, B. Targeting the Proteostasis Network for Mycobacterial Drug Discovery. *ACS Infect Dis* **4**, 478–498 (2018).

6. Li, D. *et al.* Structural basis for the assembly and gate closure mechanisms of the Mycobacterium tuberculosis 20S proteasome. *EMBO J* **29**, 2037–2047 (2010).
7. Hu, K. *et al.* Proteasome substrate capture and gate opening by the accessory factor PafE from Mycobacterium tuberculosis. *J Biol Chem* **293**, 4713–4723 (2018).
8. Lin, G. *et al.* Mycobacterium tuberculosis prcBA genes encode a gated proteasome with broad oligopeptide specificity. *Molecular Microbiology* **59**, 1405–1416 (2006).
9. Kavalchuk, M., Jomaa, A., Müller, A. U. & Weber-Ban, E. Structural basis of prokaryotic ubiquitin-like protein engagement and translocation by the mycobacterial Mpa-proteasome complex. *Nat Commun* **13**, 276 (2022).
10. Xiao, X. *et al.* The β-Grasp Domain of Proteasomal ATPase Mpa Makes Critical Contacts with the Mycobacterium tuberculosis 20S Core Particle to Facilitate Degradation. *mSphere* **7**, e00274-22 (2022).
11. Jastrab, J. B. *et al.* An adenosine triphosphate-independent proteasome activator contributes to the virulence of *Mycobacterium tuberculosis*. *Proc. Natl. Acad. Sci. U.S.A.* **112**, (2015).
12. Bai, L. *et al.* Structural analysis of the dodecameric proteasome activator PafE in Mycobacterium tuberculosis. *Proceedings of the National Academy of Sciences* **113**, E1983–E1992 (2016).
13. Bolten, M. *et al.* Structural Analysis of the Bacterial Proteasome Activator Bpa in Complex with the 20S Proteasome. *Structure* **24**, 2138–2151 (2016).
14. Delley, C. L. *et al.* Bacterial Proteasome Activator Bpa (Rv3780) Is a Novel Ring-Shaped Interactor of the Mycobacterial Proteasome. *PLoS One* **9**, e114348 (2014).
15. Jastrab, J. B., Samanovic, M. I., Copin, R., Shopsin, B. & Darwin, K. H. Loss-of-Function Mutations in HspR Rescue the Growth Defect of a Mycobacterium tuberculosis Proteasome Accessory Factor E (pafE) Mutant. *Journal of Bacteriology* **199**, 10.1128/jb.00850-16 (2017).

16. Parijat, P. & Batra, J. K. Role of DnaK in HspR-HAIR interaction of ycobacterium tuberculosis. *IUBMB Life* **67**, 816–827 (2015).

17. Bucca, G., Brassington, A. M., Schönfeld, H. J. & Smith, C. P. The HspR regulon of Streptomyces coelicolor: a role for the DnaK chaperone as a transcriptional co-repressordagger. *Mol Microbiol* **38**, 1093–1103 (2000).

18. Striebel, F., Hunkeler, M., Summer, H. & Weber-Ban, E. The mycobacterial Mpa–proteasome unfolds and degrades pupylated substrates by engaging Pup's N-terminus. *EMBO J* **29**, 1262–1271 (2010).

19. Pearce, M. J. *et al.* Identification of substrates of the Mycobacterium tuberculosis proteasome. *EMBO J* **25**, 5423–5432 (2006).

20. Elharar, Y. *et al.* Posttranslational regulation of coordinated enzyme activities in the Pup-proteasome system. *Proc Natl Acad Sci U S A* **113**, E1605-1614 (2016).

21. von Rosen, T. *et al.* Substrates bind to residues lining the ring of asymmetrically engaged bacterial proteasome activator Bpa. *Nat Commun* **16**, 3042 (2025).

22. Davis, B. T. V., Velyvis, A. & Vahidi, S. Fluorinated Ethylamines as Electrospray-Compatible Neutral pH Buffers for Native Mass Spectrometry. *Anal. Chem.* **95**, 17525–17532 (2023).

23. Liu, R., Li, Q. & Smith, L. M. Detection of Large Ions in Time-of-Flight Mass Spectrometry: Effects of Ion Mass and Acceleration Voltage on Microchannel Plate Detector Response. *J. Am. Soc. Mass Spectrom.* **25**, 1374–1383 (2014).

24. Chernushevich, I. V. & Thomson, B. A. Collisional Cooling of Large Ions in Electrospray Mass Spectrometry. *Anal. Chem.* **76**, 1754–1760 (2004).

25. Morgan, C. R. & Engen, J. R. Investigating solution-phase protein structure and dynamics by hydrogen exchange mass spectrometry. *Curr Protoc Protein Sci* **Chapter 17**, 17.6.1-17.6.17 (2009).

26. James, E. I., Murphree, T. A., Vorauer, C., Engen, J. R. & Guttman, M. Advances in Hydrogen/Deuterium Exchange Mass Spectrometry and the Pursuit of Challenging Biological Systems. *Chem Rev* **122**, 7562–7623 (2022).
27. Konermann, L., Pan, J. & Liu, Y.-H. Hydrogen exchange mass spectrometry for studying protein structure and dynamics. *Chem. Soc. Rev.* **40**, 1224–1234 (2011).
28. Konermann, L., Rodriguez, A. D. & Sowole, M. A. Type 1 and Type 2 scenarios in hydrogen exchange mass spectrometry studies on protein–ligand complexes. *Analyst* **139**, 6078–6087 (2014).
29. Bai, Y., Milne, J. S., Mayne, L. & Englander, S. W. Primary structure effects on peptide group hydrogen exchange. *Proteins* **17**, 75–86 (1993).
30. Nguyen, D., Mayne, L., Phillips, M. C. & Walter Englander, S. Reference Parameters for Protein Hydrogen Exchange Rates. *J Am Soc Mass Spectrom* **29**, 1936–1939 (2018).
31. Vorauer, C. *et al.* Rapid Assessment of Pepsin Column Activity for Reliable HDX-MS Studies. *J Am Soc Mass Spectrom* **32**, 2386–2390 (2021).
32. Yang, M. *et al.* Recombinant Nepenthesin II for Hydrogen/Deuterium Exchange Mass Spectrometry. *Anal. Chem.* **87**, 6681–6687 (2015).
33. Peterle, D., DePice, D., Wales, T. E. & Engen, J. R. Increase the flow rate and improve hydrogen deuterium exchange mass spectrometry. *Journal of Chromatography A* **1689**, 463742 (2023).
34. Hodge, E. A., Benhaim, M. A. & Lee, K. K. Bridging protein structure, dynamics, and function using hydrogen/deuterium-exchange mass spectrometry. *Protein Sci* **29**, 843–855 (2020).
35. Vosper, K. R., Velyvis, A. & Vahidi, S. HDgraphiX: A Web-Based Tool for Visualization of Hydrogen/Deuterium Exchange Mass Spectrometry Data. *J. Am. Soc. Mass Spectrom.* **36**, 1200–1203 (2025).

36. Tugarinov, V., Hwang, P. M., Ollerenshaw, J. E. & Kay, L. E. Cross-Correlated Relaxation Enhanced 1H−13C NMR Spectroscopy of Methyl Groups in Very High Molecular Weight Proteins and Protein Complexes. *J. Am. Chem. Soc.* **125**, 10420–10428 (2003).

37. Rosenzweig, R. & Kay, L. E. Bringing Dynamic Molecular Machines into Focus by Methyl-TROSY NMR. *Ann. Rev. Biochem.* **83**, 291–315 (2014).

38. Schütz, S. & Sprangers, R. Methyl TROSY spectroscopy: A versatile NMR approach to study challenging biological systems. *Progress in Nuclear Magnetic Resonance Spectroscopy* https://doi.org/10.1016/j.pnmrs.2019.09.004 (2019) doi:10.1016/j.pnmrs.2019.09.004.

39. Sprangers, R., Velyvis, A. & Kay, L. E. Solution NMR of supramolecular complexes: providing new insights into function. *Nature Methods* **4**, 697–703 (2007).

40. Evans, R., Dal Poggetto, G., Nilsson, M. & Morris, G. A. Improving the Interpretation of Small Molecule Diffusion Coefficients. *Anal. Chem.* **90**, 3987–3994 (2018).

41. Valencia, D. P. & González, F. J. Estimation of diffusion coefficients by using a linear correlation between the diffusion coefficient and molecular weight. *Journal of Electroanalytical Chemistry* **681**, 121–126 (2012).

42. Goodhill, G. J. Mathematical guidance for axons. *Trends in Neurosciences* **21**, 226–231 (1998).

43. Nishikawa, T., Nagadoi, A., Yoshimura, S., Aimoto, S. & Nishimura, Y. Solution structure of the DNA-binding domain of human telomeric protein, hTRF1. *Structure* **6**, 1057–1065 (1998).

44. Sekhar, A., Rosenzweig, R., Bouvignies, G. & Kay, L. E. Mapping the conformation of a client protein through the Hsp70 functional cycle. *Proceedings of the National Academy of Sciences* **112**, 10395–10400 (2015).

45. Rosenzweig, R., Sekhar, A., Nagesh, J. & Kay, L. E. Promiscuous binding by Hsp70 results in conformational heterogeneity and fuzzy chaperone-substrate ensembles. *Elife* **6**, e28030 (2017).

46. Sekhar, A., Nagesh, J., Rosenzweig, R. & Kay, L. E. Conformational heterogeneity in the Hsp70 chaperone-substrate ensemble identified from analysis of NMR-detected titration data. *Protein Sci* **26**, 2207–2220 (2017).

47. Sekhar, A., Rosenzweig, R., Bouvignies, G. & Kay, L. E. Hsp70 biases the folding pathways of client proteins. *Proc Natl Acad Sci U S A* **113**, E2794-2801 (2016).

48. Harkness, R. W. *et al.* Competing stress-dependent oligomerization pathways regulate self-assembly of the periplasmic protease-chaperone DegP. *Proc Natl Acad Sci U S A* **118**, e2109732118 (2021).

49. Harkness, R. W., Ripstein, Z. A., Di Trani, J. M. & Kay, L. E. Flexible Client-Dependent Cages in the Assembly Landscape of the Periplasmic Protease-Chaperone DegP. *J. Am. Chem. Soc.* **145**, 13015–13026 (2023).

50. Turner, M. *et al.* Structural basis for allosteric modulation of M. tuberculosis proteasome core particle. *Nat Commun* **16**, 3138 (2025).

51. Yuwen, T., Sekhar, A., Baldwin, A. J., Vallurupalli, P. & Kay, L. E. Measuring Diffusion Constants of Invisible Protein Conformers by Triple-Quantum 1H CPMG Relaxation Dispersion. *Angewandte Chemie International Edition* **57**, 16777–16780 (2018).

52. Kramer, A., Schwebke, I. & Kampf, G. How long do nosocomial pathogens persist on inanimate surfaces? A systematic review. *BMC Infect Dis* **6**, 130 (2006).

53. Qi, D. & Scholthof, K.-B. G. A one-step PCR-based method for rapid and efficient site-directed fragment deletion, insertion, and substitution mutagenesis. *J Virol Methods* **149**, 85–90 (2008).

54. Tugarinov, V., Hwang, P. M. & Kay, L. E. Nuclear magnetic resonance spectroscopy of high-molecular-weight proteins. *Annu Rev Biochem* **73**, 107–146 (2004).

55. Laemmli, U. K. Cleavage of Structural Proteins during the Assembly of the Head of Bacteriophage T4. *Nature* **227**, 680–685 (1970).

56. Kalambet, Y., Kozmin, Y., Mikhailova, K., Nagaev, I. & Tikhonov, P. Reconstruction of chromatographic peaks using the exponentially modified Gaussian function. *Journal of Chemometrics* **25**, 352–356 (2011).

57. Glasoe, P. K. & Long, F. A. USE OF GLASS ELECTRODES TO MEASURE ACIDITIES IN DEUTERIUM OXIDE1,2. *J. Phys. Chem.* **64**, 188–190 (1960).

58. Vahidi, S., Bi, Y., Dunn, S. D. & Konermann, L. Load-dependent destabilization of the γ-rotor shaft in FOF1 ATP synthase revealed by hydrogen/deuterium-exchange mass spectrometry. *Proceedings of the National Academy of Sciences* **113**, 2412–2417 (2016).

59. Sørensen, L. & Salbo, R. Optimized Workflow for Selecting Peptides for HDX-MS Data Analyses. *J. Am. Soc. Mass Spectrom.* **29**, 2278–2281 (2018).

60. Meng, E. C. *et al.* UCSF ChimeraX: Tools for structure building and analysis. *Protein Science* **32**, e4792 (2023).

61. Marty, M. T. *et al.* Bayesian Deconvolution of Mass and Ion Mobility Spectra: From Binary Interactions to Polydisperse Ensembles. *Anal. Chem.* **87**, 4370–4376 (2015).

62. Todd, A. R. & Jarrold, M. F. Dramatic Improvement in Sensitivity with Pulsed Mode Charge Detection Mass Spectrometry. *Anal. Chem.* **91**, 14002–14008 (2019).

63. Delaglio, F. *et al.* NMRPipe: a multidimensional spectral processing system based on UNIX pipes. *J Biomol NMR* **6**, 277–293 (1995).

64. Kay, L. E., Keifer, P. & Saarinen, T. Pure absorption gradient enhanced heteronuclear single quantum correlation spectroscopy with improved sensitivity. *J. Am. Chem. Soc.* **114**, 10663–10665 (1992).

65. Choy, W.-Y. *et al.* Distribution of molecular size within an unfolded state ensemble using small-angle X-ray scattering and pulse field gradient NMR techniques. *J Mol Biol* **316**, 101–112 (2002).

66. Bouvignies, G. & Kay, L. E. A 2D ^{13}C-CEST experiment for studying slowly exchanging protein systems using methyl probes: an application to protein folding. *J Biomol NMR* **53**, 303–310 (2012).

67. Yuwen, T., Kay, L. E. & Bouvignies, G. Dramatic Decrease in CEST Measurement Times Using Multi-Site Excitation. *Chemphyschem* **19**, 1707–1710 (2018).

68. Korzhnev, D. M., Kloiber, K., Kanelis, V., Tugarinov, V. & Kay, L. E. Probing Slow Dynamics in High Molecular Weight Proteins by Methyl-TROSY NMR Spectroscopy: Application to a 723-Residue Enzyme. *J. Am. Chem. Soc.* **126**, 3964–3973 (2004).

69. Tanford, Charles. Contribution of Hydrophobic Interactions to the Stability of the Globular Conformation of Proteins. *J. Am. Chem. Soc.* **84**, 4240–4247 (1962).

Acknowledgements

B.T.V.D. acknowledges support from a Graduate Tuition Scholarship from the University of Guelph. Financial support was provided by Canadian Institutes of Health Research Project Grant PJT451412 to S.V. and a Foundation Grant FND-503573 to L.E.K., and by a Discovery Grant from the Natural sciences and Engineering Council of Canada RGPIN-2021-02843 to S.V and 024-03872 to L.E.K. MS data were recorded at the Mass Spectrometry Facility of the Advanced Analysis Centre, University of Guelph. We thank Dr. Dyanne Brewer (University of Guelph) for assistance with MS measurements. We thank Prof. Ashok Sekhar (Indian Institute of Science Bangalore) for providing backbone resonance assignments of TRF1. We thank Dr. Taylor Forrester (University of Guelph) for help with the generation of the protein topology diagrams. We thank Dr. Algirdas Velyvis (University of Guelph) for guidance and helpful discussions.

Statement of contribution

B.T.V.D., E.R., L.E.K., and S.V. initiated the project; B.T.V.D., E.R., L.E.K., and S.V. designed research; B.T.V.D., E.R., A.H., J.U., L.E.K., and S.V. performed research; B.T.V.D., E.R., A.H., J.U., D.B., K.R., K.G., L.E.K., and S.V. contributed new reagents/analytic tools; B.T.V.D., E.R., A.H., and S.V. analyzed data; B.T.V.D., E.R., L.E.K., and S.V. wrote the paper.

Competing interests

A.H, J.U, D.B, K.R, K.G are employees of Waters Corporation, whose instrumentation was used in this study. Waters provided technical support, including access to software and, in the case of CD-MS, the prototype instrument itself, enabling nonconventional experiments to be performed. However, the company did not participate in experimental design, data interpretation, or manuscript preparation. The remaining authors declare no competing interests.

Figure legends

Figure 1. Bpa undergoes a temperature-dependent oligomerization. a) Cartoon representation of an unbound 20S CP (PDB: 9CE5)[50]. The expanded box depicts the closed gate conformation of the gating residues (PDB: 6BGO)[7]; (**b**) Density map of Bpa bound to the 20S CP (EMDB: 19150)[21]. The expanded box highlights the open-gate conformation induced by insertion of the Bpa C-terminal GQYL motif into a pocket formed at the interface between adjacent subunits of the α_7-ring (PDB: 6BGO)[7]; (**c**) Cartoon representation of an individual Bpa subunit, highlighting the four-helix bundle fold and the flexible C-terminal region containing the

^{171}GQYL^{174} motif. Residues 145-174 are not resolved in the crystal structure (PDB ID: 5LFJ)[13]; (**d**) Top and side view of an individual Bpa subunit (cartoon) within the 227.3 kDa homododecameric Bpa ring (surface); (**e**) SEC chromatograms indicating a shift in the Bpa oligomeric equilibrium as a function of incubation time (37 °C), after equilibration of Bpa at 4 °C. The large molecular weight (MW) species is denoted as P1 (peak 1), while the two lower MW species are denoted as P2 and P3 (peaks 2 and 3); (**f**) Changes in the fractional populations of the P1 (red) and P2+P3 (blue) species from analysis using an exponential decay model to extract an association rate (*k*). Residuals of the decay model fitting are displayed in the plot above. Mean population values and uncertainties of P1 and P2+P3 populations were calculated via bootstrapping in which 5% of the chromatographic data was resampled and independently fit (n = 1000). ; (**g**) Nano-ESI native MS displays changes in the oligomeric equilibrium of Bpa upon incubation at 37 °C, starting from a distribution that was generated at 4 °C. The species in solution were identified as dodecameric (P1), tetrameric (P2), and dimeric (P3) Bpa oligomers. All spectra were normalized to the highest intensity peak in each spectrum, with these values given in the top left corner. The predominant charge state for each species is denoted on the 24 h spectrum; and (**h**) CD-MS analysis of Bpa incubated overnight at 37 °C shows that WT Bpa predominantly adopts a dodecameric state. Source data are provided as a Source Data file.

Figure 2. Pulsed HDX-MS reveals the time-dependent evolution of structure during dodecameric Bpa assembly. (**a**) Heatmap showing differential deuterium uptake following a 10-second D_2O pulse at various time points during Bpa assembly, relative to the onset of the assembly reaction (*t* = 0 h). Bpa secondary structure elements and their corresponding residue numbers are denoted along the top of the heatmap; Side (**b**) and top views (**c**) of Bpa, shown as surface representations, with one subunit displayed as a cartoon (PDB: 5LFJ)[13]. Differential

deuterium uptake is mapped onto the cartoon subunit. Structural figure panels were generated using ChimeraX 1.90[60].

Figure 3. Bpa oligomerization interfaces exhibit asymmetric isotopic distributions during assembly, as revealed by pulsed HDX-MS. (**a**) A pair of Gaussian functions were fit to intensity profiles from peptides displaying asymmetric isotopic distributions and subsequently integrated. Closed (low HDX - red) and open (high HDX - teal) conformations and their fractional populations are denoted in the raw mass spectra. The displayed peptides are representative of others across the sequence but were selected to maximize sequence coverage; (**b**) Assembly time-dependent changes in the fractional populations of the open and closed conformations for two representative peptides were analyzed using a single-exponential decay model to extract the association rate constant (*k*). Data points represent the mean populations fractions averaged across technical replicates (n=3), with error bars representing standard deviation.; and (**c**) Association rate constants *k* extracted from all peptides exhibiting EX1 kinetics. Data points and error bars were calculated in the same manner listed above. The hatched horizontal grey line denotes the association rate constant determined from SEC measurements, with the shaded region indicating ±2σ. Although the data were not globally fit, the similar *k* values across peptides suggest they report on a common underlying process, namely the formation of dodecameric Bpa.

Figure 4. N- and C- terminal truncations stabilize specific oligomeric forms of Bpa. (**a**) ^{1}H-^{13}C HMQC spectra for ILVM-labeled Bpa $_{WT}$ preincubated at 4 °C (multi-contour blue) or 40 °C (multi-contour red), Bpa $_{31\text{-}146}$ (single-contour red), and Bpa $_{45\text{-}153}$ (single-contour blue). All spectra were recorded at 40 °C and 18.8 T; (**b**) Changes in peak intensity for each oligomeric

state (tetramer - blue, dodecamer - red) during a 48-hour acquisition. Data were fit assuming a first-order exponential model. Residuals are displayed in the plot above; and (**c**) Intensity ratios of selected peaks (see Supplemental Methods) as a function of gradient strength (G) recorded in a pulsed-field gradient diffusion experiment[65] (circles). Intensities for a given value of G are normalized to their values obtained with the lowest value of G used in the experiments and fit (solid lines) to extract diffusion coefficients (D). Diffusion coefficients of Bpa $_{WT}$ for each oligomeric state (tetramer - blue, dodecamer - red) are indicated.

Figure 5. hTRF1 interacts with the C-terminal residues in the lower inner ring of dodecameric Bpa. Assigned (**a**) Met, (**b**) Ile, and (**c**) Leu/Val regions of a two-dimensional ^{1}H-^{13}C HMQC spectrum for ILVM-labeled Bpa recorded at 40 °C and 18.8 T. Peaks depicted with dark purple contours are derived from apo Bpa and those with light purple contours from a complex of Bpa and [U-^{2}H] hTRF1 in molar ratios of 100 μM (subunit concentration of Bpa): 150 μM (hTRF1) in the presence of 300 mM KCl; (**d**) Top view of the Bpa complex highlighting the inner and outer ring architecture. The inset shows a single Bpa subunit in cartoon representation highlighting residues, shown as grey sticks, that display CSPs upon hTRF1 binding (PDB: 5LFJ)[13]. The sole charged residues proximal to these residues are shown in red and blue; (**e**) Isolated regions of the ^{1}H-^{13}C HMQC spectrum for residues showing major chemical shift changes upon hTRF1 addition; (**f**) Titration of [U-^{2}H] hTRF1 with ILVM-labelled Bpa at 50 mM KCl, monitoring ^{1}H or ^{13}C chemical shift changes; and (**g**) Titration of ILVM-labelled Bpa with [U-^{2}H] hTRF1 at 300 mM KCl, monitoring ^{1}H or ^{13}C chemical shift changes. Black circles in (f) and (g) denote best-fit peak positions obtained using the nonlinear N-dimensional spectral modeling routine (nlinLS) in NMRPipe. Error bars represent the root-mean-square deviation of

experimental peak positions from a preliminary fit to a single-site binding isotherm in which the effective [Bpa] was treated as a fitted parameter.

Figure 6. Hydrophobic patches and charged residues on hTRF1 mediate Bpa binding. (a) Superposition of ^{1}H-^{15}N HSQC spectra of [U-^{15}N]-labeled hTRF1 in the absence and presence of 10-fold monomer equivalents of unlabelled Bpa $_{31\text{-}146}$ measured in the presence of 300 mM KCl, 40 °C. Top and bottom spectra were recorded on samples of hTRF1 $_{\Delta 39\text{-}53}$ and hTRF1 $_{\Delta 20\text{-}38}$, respectively. (b) Intensity ratios for each hTRF1 peak in the absence and presence of unlabelled Bpa $_{31\text{-}146}$. The intensity ratios for each hTRF1 construct are colour-coded as indicated. The grey trace indicates the Tanford hydrophobic index[69] for the hTRF1 sequence. In the hTRF1 sequence, positively and negatively charged residues are denoted in blue and red, respectively.

Editor's Summary

Bpa (bacterial proteasome activator) is essential for *Mycobacterium tuberculosis* virulence, yet its structural heterogeneity and mode of substrate engagement have remained poorly understood. Here, the authors combine hydrogen/deuterium exchange mass spectrometry and solution NMR spectroscopy to elucidate Bpa assembly and its interaction with a model substrate.

Peer Review Information: *Nature Communications* thanks the anonymous reviewer(s) for their contribution to the peer review of this work. A peer review file is available.

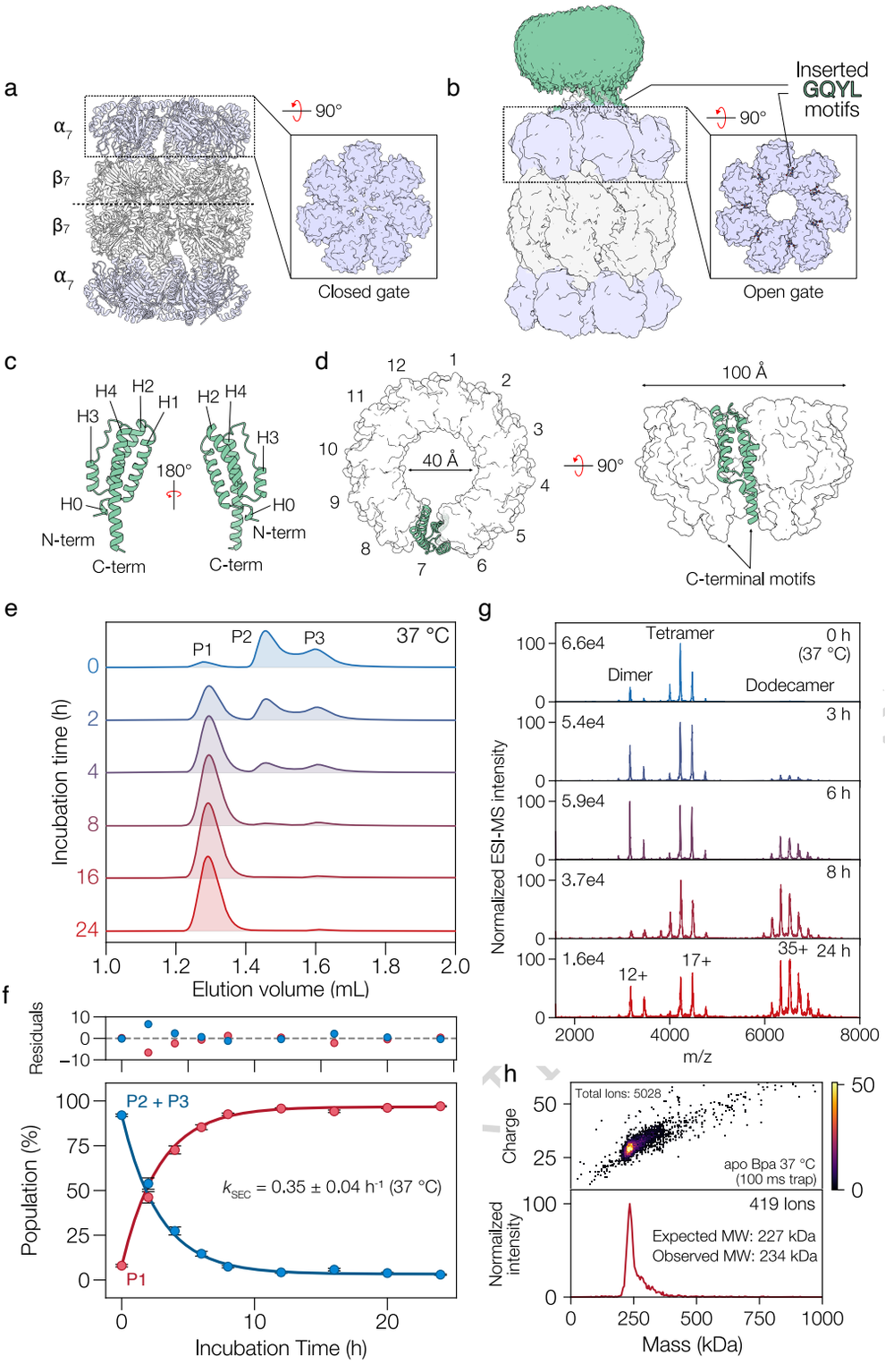
a
α7
β7
β7
α7
90°
Closed gate
b
Inserted
GQYL
motifs
90°
Open gate
c
H4
H2
H1
H3
H0
N-term
C-term
180°
H2
H4
H3
H0
N-term
C-term
d
12
1
2
3
4
5
6
7
8
9
10
11
40 Å
90°
100 Å
C-terminal motifs
e
37 °C
P1
P2
P3
0
2
4
8
16
24
Incubation time (h)
1.0
1.2
1.4
1.6
1.8
2.0
Elution volume (mL)
f
Residuals
10
0
−10
100
75
50
25
0
Population (%)
P2 + P3
P1
k_{SEC} = 0.35 ± 0.04 h⁻¹ (37 °C)
0
10
20
Incubation Time (h)
g
6.6e4
Tetramer
0 h
(37 °C)
Dimer
Dodecamer
5.4e4
3 h
5.9e4
6 h
3.7e4
8 h
1.6e4
12+
17+
35+
24 h
Normalized ESI-MS intensity
2000
4000
6000
8000
m/z
h
Total Ions: 5028
Charge
50
25
apo Bpa 37 °C
(100 ms trap)
50
0
419 Ions
Expected MW: 227 kDa
Observed MW: 234 kDa
Normalized intensity
0
250
500
750
1000
Mass (kDa)

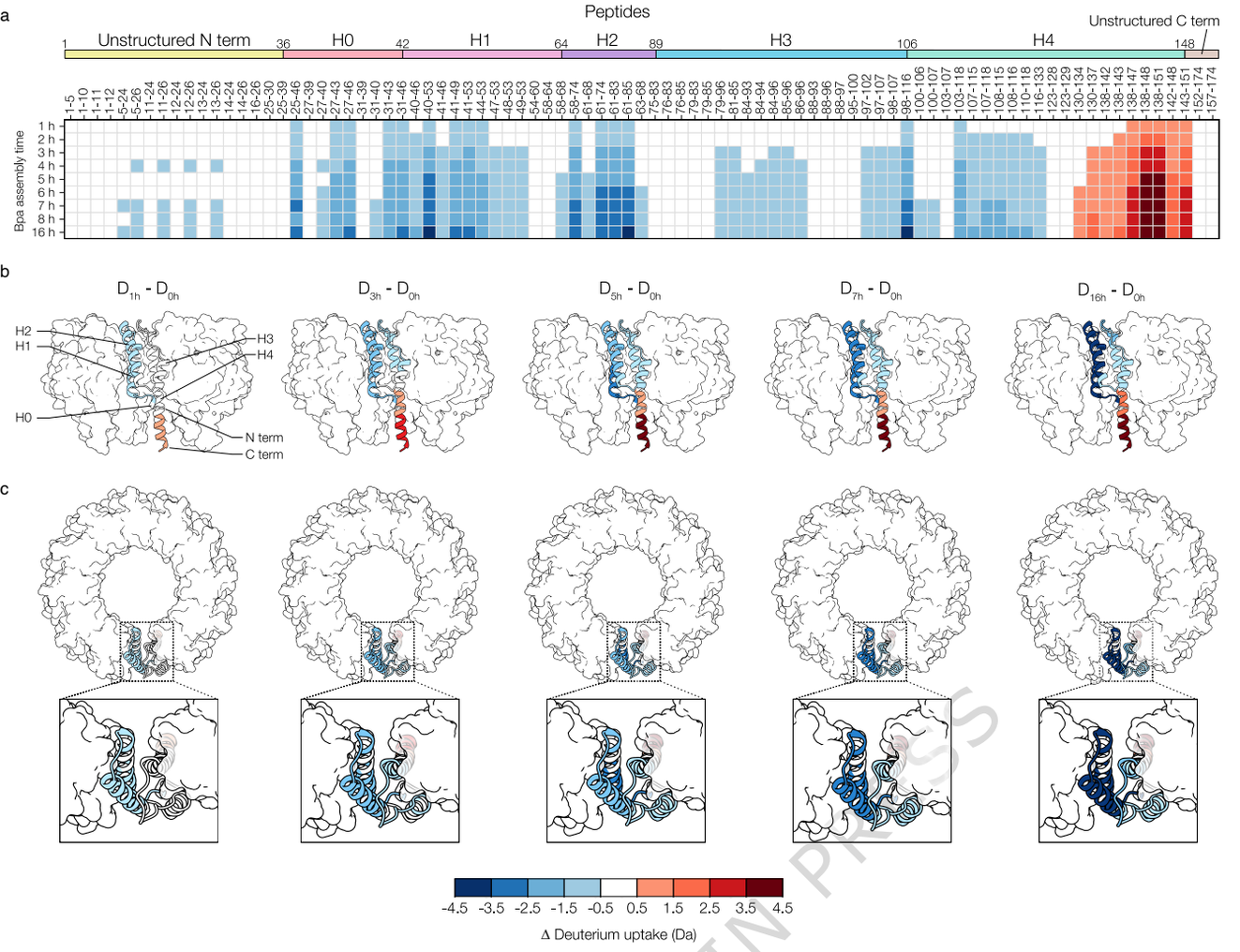

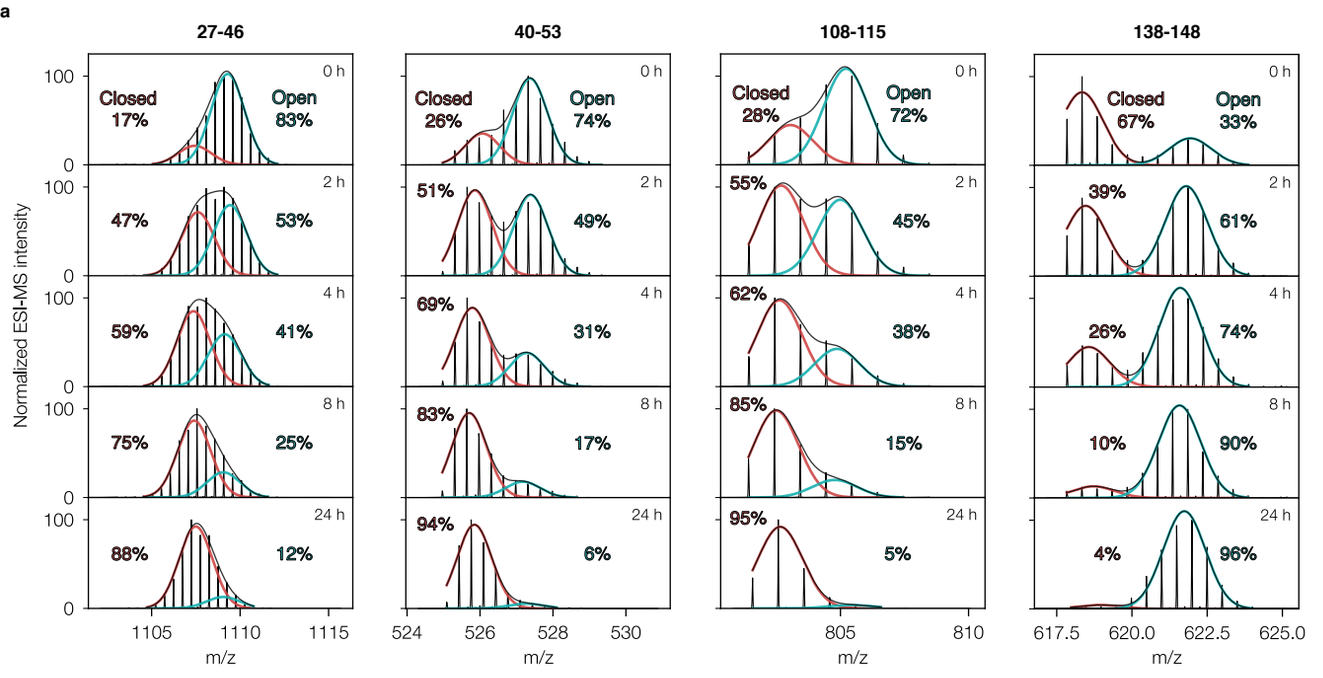

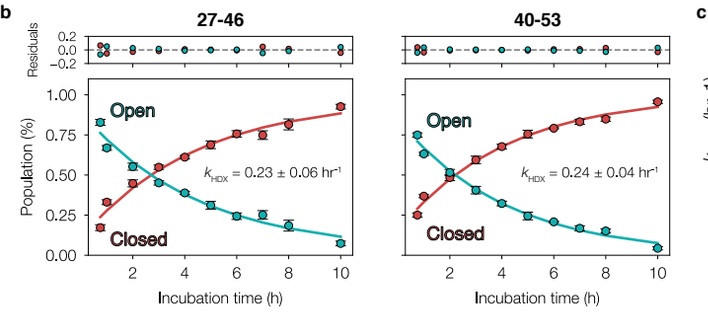

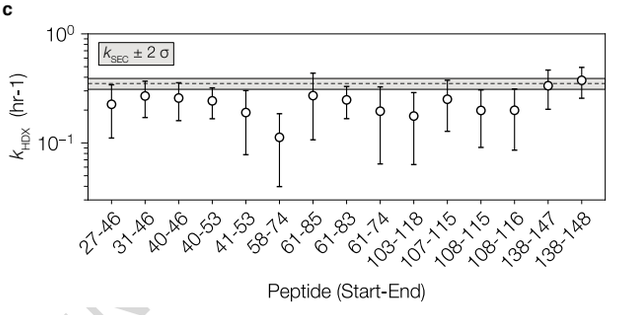

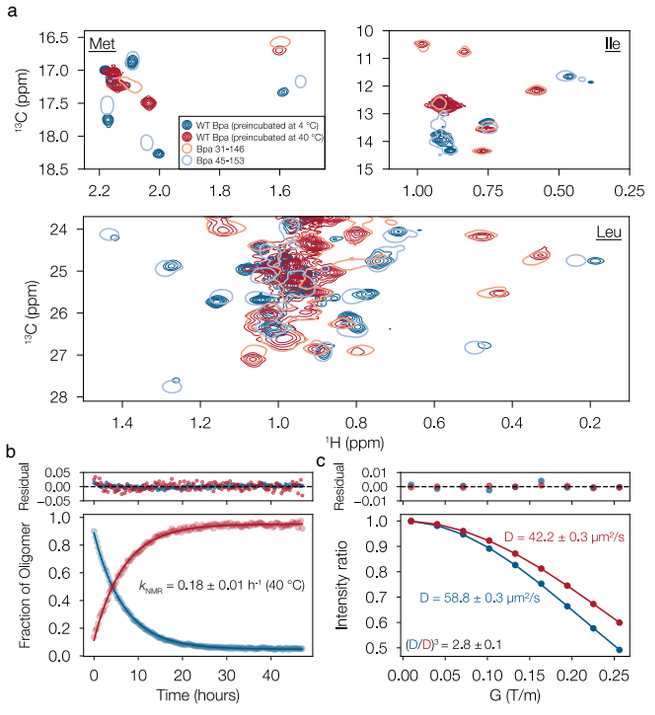

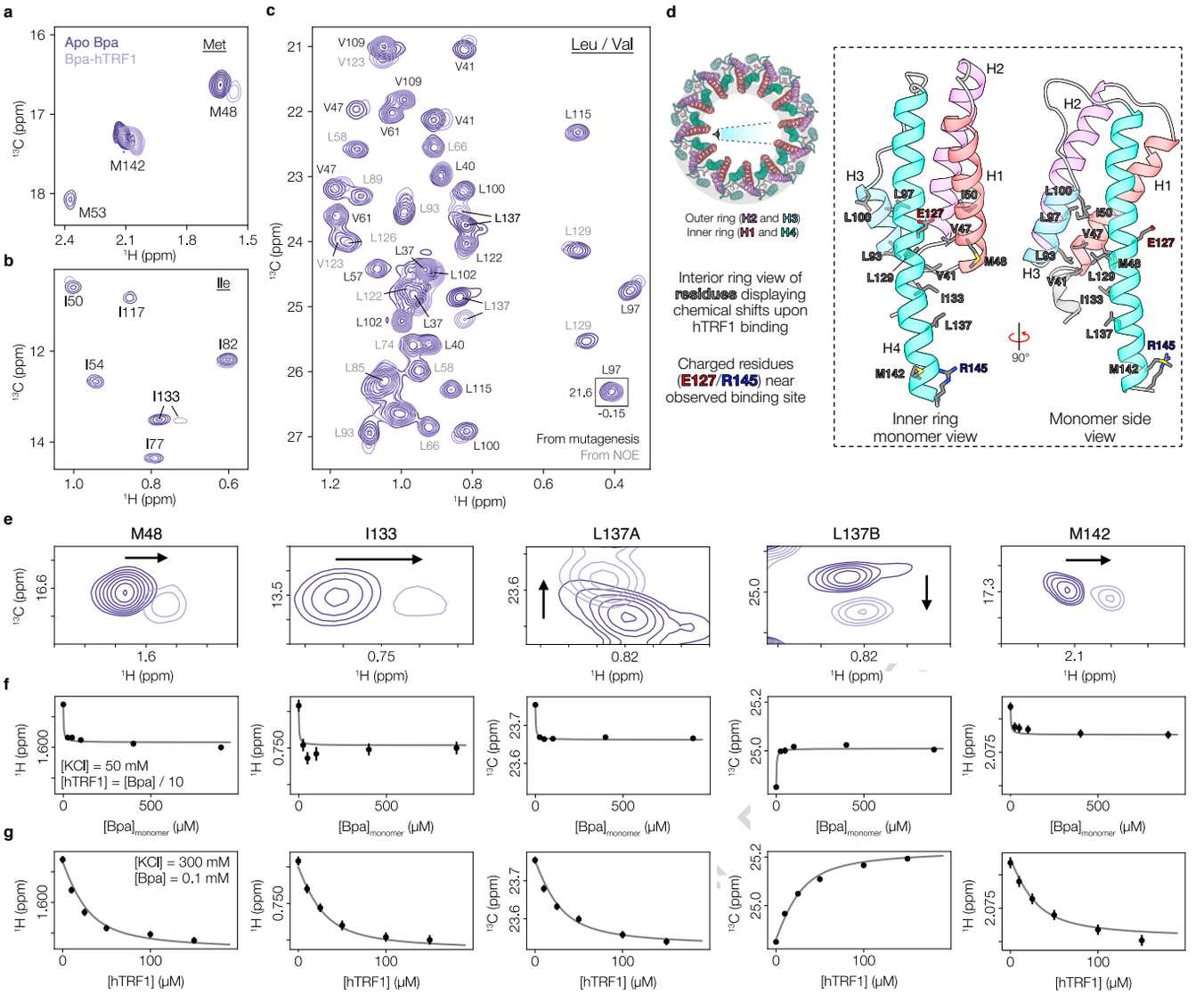
a
Apo Bpa
Bpa-hTRF1
Met
M48
M142
M53
^{13}C (ppm)
^{1}H (ppm)
b
Ile
I50
I117
I82
I54
I133
I77
c
Leu / Val
From mutagenesis
From NOE
d
Outer ring (H2 and H3)
Inner ring (H1 and H4)
Interior ring view of residues displaying chemical shifts upon hTRF1 binding
Charged residues (E127/R145) near observed binding site
Inner ring monomer view
Monomer side view
90°
e
M48
I133
L137A
L137B
M142
f
[KCl] = 50 mM
[hTRF1] = [Bpa] / 10
[Bpa]$_{monomer}$ (μM)
g
[KCl] = 300 mM
[Bpa] = 0.1 mM
[hTRF1] (μM)